Supplementary Information

A giant galaxy in the young Universe with a massive ring

Tiantian Yuan[1,2,*], Ahmed Elagali[3,2], Ivo Labbe[1], Glenn G. Kacprzak[1,2], Claudia del P. Lagos[3,2,4], Leo Y. Alcorn[5,6], Jonathan H. Cohn[5], Kim-Vy H. Tran[5,7,2], Karl Glazebrook[1,2], Brent A. Groves[3,8,2], Kenneth C. Freeman[8], Lee R. Spitler[9,10,2], Caroline M. S. Straatman[11], Deanne B. Fisher[1], Sarah M. Sweet[1,2,12]

[1]Centre for Astrophysics and Supercomputing, Swinburne University of Technology, Hawthorn, Victoria 3122, Australia. [2]ARC Centre of Excellence for All Sky Astrophysics in 3 Dimensions (ASTRO 3D), Australia. [3]International Centre for Radio Astronomy Research (ICRAR), M468, The University of Western Australia, 35 Stirling Highway, Crawley, WA 6009, Australia. [4]Cosmic Dawn Center (DAWN), Denmark. [5]George P. and Cynthia Woods Mitchell Institute for Fundamental Physics and Astronomy, Department of Physics & Astronomy, Texas A&M University, College Station, TX, 77843, USA. [6]Department of Physics and Astronomy, York University, 4700 Keele St., Toronto, Ontario, Canada, MJ3 1P3. [7]School of Physics, University of New South Wales, NSW 2052, Australia. [8]Research School of Astronomy and Astrophysics, the Australian National University, Canberra, ACT 2611, Australia. [9]Research Centre for Astronomy, Astrophysics & Astrophotonics, Macquarie University, Sydney, NSW 2109, Australia. [10]Department of Physics & Astronomy, Macquarie University, Sydney, NSW 2109, Australia. [11]Sterrenkundig Observatorium, Universiteit Gent, Krijgslaan 281 S9, 9000 Gent, Belgium. [12]School of Mathematics and Physics, University of Queensland, Brisbane, Qld 4072, Australia

SUPPLEMENTARY NOTES

To support our analysis and conclusions in the Letter and the Methods, this supplementary information includes 10 sections with 16 Supplementary Figures and 4 Tables.

We present more details about our observations and data reduction in Section 1 and analysis of multi-wavelength imaging data in Section 2. The ISM properties are derived in Section 3. Discussions on systematic uncertainties associated with our stellar mass and kinematic modelling are presented in Section 4 and 5, respectively. The collisional ring time scale is estimated in Section 6. Our analysis on a $z \sim 2$ ring galaxy in EAGLE simulations is presented in Section 7. We discuss alternative origins of R5519 in Section 8. The implied number density of CRGs at $z \sim 2$ is discussed in Section 9 and we provide possible explanations for the number density evolution of CRGs with redshift in Section 10.

1 Observations and Data Reduction

1.1 Keck/MOSFIRE Slit Spectroscopy Spectroscopic data from the MOSFIRE instrument[1] were obtained on the Keck 1 telescope on Mauna Kea on the 13th of February 2017 (Project Code: Z245). We observed in the K-band with a spectral resolution of $R = 3610$ (i.e., velocity resolution of $\sigma_v = 35$ km/s). An AB dithering pattern with 1.5 arcsecond length was used. The PA of the slits is 58°. The total exposure on the mask was 96 minutes. The average seeing was $0\farcs8$ during the integration of this particular mask, equivalent to the slit width.

We reduce the data using a similar procedure as our ZFIRE survey[2]. In summary, we use the MOSFIRE data reduction pipeline (DRP) for initial 2D data processing including flat-fielding, spatial rectification, sky subtraction, and wavelength calibration. The wavelength calibration is carried out in vacuum using arc and sky lines, with a typical residual of $\lesssim 0.1$Å. The DRP also generates the associated 2D 1σ spectra that we use for error analysis. An A0V type star is used for telluric and initial flux calibration. We use our customised code to implement telluric correction, flux calibration, 1D spectra extraction, and emission line profile fitting. Because R5519 is an abnormally extended object that does not follow the overall size distribution of $z \sim 2$ ZFOURGE galaxies[3], we derive the slit-loss and flux calibration correction factor independently in Methods.

The total observed 1D spectrum for R5519 is presented in Supplementary Fig.3. The emission line fitting procedure involves fitting Gaussian profiles simultaneously to three emission lines: [N II]λ6548, 6583 and Hα (Supplementary Fig.3). The [S II] doublet lines are fitted as double Gaussians separately. The line profile fitting is conducted using a χ^2 minimisation procedure weighted by the inverse of the variance spectrum. We derive a Balmer absorption correction on the Hα emission line based on the weak stellar continuum and find it to be less than $\sim 1\%$ of the observed flux. We therefore do not correct for the small Balmer absorption because the uncertainties in aperture and dust corrections are more than one order of magnitude larger. The redshift calculated from the Hα line centroid of the total 1D spectrum is $z = 2.19$ (Supplementary Table 3). We achieve a signal-to-noise ratio (SNR) of 57 on the total flux of the Hα emission line and 15 for the [N II] line.

1.2 Keck/OSIRIS Integral Field Spectroscopy In order to obtain spatially resolved Hα kinematics, we observed R5519 with the integral-field instrument OSIRIS[4] in laser guide star (LGS) adaptive optics (AO) mode[5] on the Keck I telescope on the 8th of December 2017 (Project Code: W276). A total of 2hrs were available for R5519 including standard stars and overheads.

AO with R5519 was quite challenging because the tip-tilt (TT) star had an observed magnitude of $R_{vega} \sim 19$ and was $51\farcs1$ away from the target, approaching the Keck LGS AO system limit (e.g., the faintest TT star recorded[3] for Keck LGS AO is $R_{vega} \sim 19.2$[1]). We first acquired the TT star and centred it on the OSIRIS 100mas plate in the narrow band filter Kn2 (spectral coverage: $2.036 - 2.141\mu m$, spectral resolution: ~ 3000 or velocity resolution of $\sigma_v = 42$ km/s, FOV $4.5 \times 6.4''$). We then pointed to the centre of R5519 by applying the coordinate offset from the TT star to the centre of R5519. The offset from the TT star to the IFS centre was measured using well-calibrated HST F125W, F140W, and F160W images from the CANDELS survey[6–8] and was accurate to $0\farcs06$. The final pointing of the OSIRIS field-of-view (FOV) with respect to the ZFOURGE near-IR images is shown in Fig.2. The PA of the OSIRIS is 225°. The weather during the observation was good, with a natural K-band seeing of $\sim 0\farcs7$ and an attenuation of $\lesssim 0.2$ mag. We were able to close the AO loop for 5×900s exposures on R5519 including one 900s exposure on a blank sky nearby. The net exposure on R5519 is therefore 60mins. A Gaussian fitting to

[1]https://www2.keck.hawaii.edu/optics/lgsao/performance.html

the point spread function of the TT star yields an average FWHM of $0\farcs35$, therefore the angular resolution of our AO observation is quoted as $0\farcs35$ (3.5 spaxels on the 100mas scale).

Individual exposures are first reduced using the OSIRIS DRP (version 4.1.0)[4]. We use the sky subtraction code[9] to scale the one 900s sky exposure for each of the four exposures. The DRP reassembles the raw data into a vacuum wavelength-calibrated, sky subtracted 3D datacube. We verify the OSIRIS wavelength calibration by comparing the wavelength solution of the DRP with the vacuum wavelength of sky lines[10]. We find that DRPv4.1.0 provides a good wavelength solution with an average residual of $\lesssim 0.6$Å in the Kn2 band.

Since we are mainly concerned about kinematics of Hα emission lines from the OSIRIS datacube, a first order polynomial function is fit to the continuum for each spaxel and then subtracted out from each spaxel. The subtraction of the continuum improves the removal of lenslet to lenslet variations. To align and coadd the 4 datacubes, we first manually inspect each datacube for Hα detections. We find a $\sim 4\sigma$ detection of Hα lines averaged on a particular spatial region of 3 by 3 spaxels in the first exposure. We then look for Hα detections in the same spatial regions and find a slightly lower SNR of $\sim$4, 3, and 1 in the other 3 datacubes. We shift the centre of the 3×3 spaxel box by 1-5 spaxels to inspect possible spatial offsets. The SNR of the Hα line in the box is maximised when the offset of the centre is 0-1 spaxel. We therefore conclude that the four datacube are spatially aligned within the error of 3 spaxels, i.e., about the size of the point-spread-function (PSF) of our AO observations. The final datacube is constructed by coadding the four datacubes, weighted by the SNR of the Hα line detected in the brightest region. Telluric correction and initial flux calibration are performed on the final datacube by using one A0V standard star (HIP 26934) observed immediately before the science exposure.

The astrometry of the datacube is determined using the offset position from the TT star to the centre of the IFS with the observed position angle. We then verify the astrometry by comparing the Hα 2D map with the narrow-band Hα NB209 image.

We manually inspect all spaxels on the final OSIRIS datacube. The datacube is noise-dominated and most spaxels show no Hα line detection ($< 2\sigma$) (Supplementary Fig.4). The only region that shows a bona fide (4.4σ) Hα detection remains the one box region that we use for aligning the individual exposure. This region spatially matches the brightest location in the NB209 Hα narrow-band image within $0\farcs3$. We also experiment with smoothing and adaptive coadding techniques on the datacube but with no significant improvement in detecting Hα lines in any other spatial regions. However, the Hα velocity from the single OSIRIS region provides a key constraint on the kinematic modelling of R5519. To further check the robustness of the 4.4σ detection, we use the best-fit velocity field and the NB209 Hα image to simulate the OSIRIS observations; we are able to reproduce this detection (Supplementary Fig.4).

2 Multi-wavelength Imaging Data

2.1 ZFOURGE Catalogue Images ZFOURGE targets 3 legacy fields including an area of $11'\times11'$ in the COSMOS field[11]. The survey provides deep near-IR imaging on the FourStar instrument[12] using five medium-band filters (J1, J2, J3, Hs, Hl) and one broad-band filter (Ks)[13]. Ancillary photometric data providing additional 30 passbands from 0.38μm to 8μm are included in the survey catalogue. Comprehensive descriptions on the ZFOURGE data products can be found in the ZFOURGE survey paper[14] and in related publications[15–17].

The ZFOURGE 2017 data release provides 32 of the 36 passbands images from the U band to the Ks band. Some of these passbands overlap. ZFOURGE catalogue images are fully reduced, calibrated and interpolated on a pixel grid of $0\farcs15$. ZFOURGE also provides a super deep K-band detection image (Ks_{tot}) by combining FourStar/Ks-band observations with pre-existing K-band images from other catalogues. The average PSF of the Ks_{tot} image is FWHM $\sim 0\farcs47$. Note that the far-IR Spitzer/MIPS and Herschel/PACS images exist for R5519 but are not included in the current ZFOURGE data release. Because of the large PSF of the far-IR images, the images of R5519 and its neighbouring galaxy G5593 are blended. We do not include the far-IR images in our current analysis.

The ring structure has the highest contrast in the HST F125W and F160W IR broad bands. At the spectroscopic redshift of R5519, the F125W band covers the strong emission line [O II]λ3727, and the F160W band contains [O III]λ5007 and Hβ emission lines. Note that because the Hα emission line falls in the middle of the NB209 narrow-band filter, the NB209 image is effectively a narrow-band image for the Hα and [N II] lines (Supplementary Fig.3). We refer to the NB209 filter image as the Hα narrow band image. We divide the 32 ZFOURGE passband images into three wavelength bins that correspond to the rest-frame FUV, NUV, and optical bands of R5519. We then stack images in these 3 bins after normalising the counts of the images to 1 and weighting the images by the inverse of the variance. The stacked images are shown on panel-c of Fig.1.

2.2 Photometry ZFOURGE provides the aperture ($1\farcs2$ diameter) and total photometry from 36 passbands, using PSF matched images[14,18]. The PSF matched images are generated by the ZFOURGE team using a Moffat profile with FWHM of $0\farcs9$ and $\beta = 0.9[ref.14]$. A FWHM of $0\farcs9$ matches the poorest image resolution of ground-based images (e.g., U and G band). The total photometry in the ZFOURGE catalogue is derived by applying an aperture correction factor (4.02 for R5519) based on the deep Ks band image profile. The total flux is the aperture flux multiplied by the correction factor. The same correction factor is applied to all passbands. This method is robust for most $z\sim2$ galaxies. However, R5519 is more extended and asymmetric (Supplementary Fig.2) than a general $z\sim2$ galaxy. To be cautious, we remeasure the photometry of R5519 based on a $2\farcs1$ diameter aperture on 32 PSF matched multi-band images. We do not include the 4 MIPS and PACS images because of their large PSFs may cause contaminations from G5593. We find that our $2\farcs1$ diameter aperture photometry and the ZFOURGE total photometry yield similar constraints on the SED fitting parameters as described in Section 4 below.

3 ISM properties

3.1 Metallicity: Global Average The global 1D MOSFIRE spectrum is extracted using an aperture of diameter $D = 2\farcs8$ (see the total spectrum in Supplementary Fig.3). The line fluxes for [N II]λ6584, H$\alpha\,\lambda$6563, [S II]λ6717,6731 are measured on the global 1D spectrum and presented in Supplementary Table 3.

We applied two empirical metallicity calibrations to derive the globally averaged gas-phase oxygen abundance (12 + log(O/H)). We first use the N2 = log([N II]λ6583/Hα) index calibrated by the PP04N2 method[19]. The PP04N2 yields $12 + \log(O/H) = 8.62 \pm 0.02$. The N2 index is the most commonly used diagnostic at high redshift because the adjacency of the [N II] and Hα lines makes the measurement efficient and unaffected by reddening. The PP04N2 method is calibrated based on local H II regions and does not consider that high-redshift galaxies may have different ionisation parameter, ISM pressure and prevalence of shocks to the low-redshift H II regions[20,21]. A recent diagnostic utilising the ratios of [N II]/[S II] and [N II]/Hα has been proposed (the D16N2S2 method[22]). The D16N2S2 method has a similar efficiency as the PP04N2 method, but is independent of varying ionisation parameters and the ISM pressure, so is ideal for determining metallicity in high-redshift galaxies. The metallicity for R5519 is calculated to be $12 + \log(O/H) = 8.92 \pm 0.06$ based on the D16N2S2 method. The errors are calculated by propagating the statistical uncertainties of the flux measurements.

The metallicity calibration of the PP04N2 method has a 1σ dispersion of 0.18 dex[19,23]; we therefore do not discuss any systematic/statistical discrepancies below this metallicity calibration uncertainty. Note that the D16N2S2 method uses a solar metallicity of 8.77 and the PP04N2 uses a solar metallicity of 8.69, causing a systematic difference of 0.08 between the two methods. However, the D16N2S2 method yields a metallicity that is 0.3 dex higher, significantly more than the scatter and the solar metallicity offset of the PP04N2 method.

Based on the PP04N2 method, R5519 has similar metallicity (within the $\sim$0.18 dex calibration uncertainty) compared with other samples of $z \sim 2$ star-forming galaxies of similar masses[24,25]. However, based on the D16N2S2 method, R5519 is as metal-enriched as a $z \sim 0$ galaxy of the same mass[26]. The different conclusions from these two methods highlight the disadvantage of the PP04N2 method to account for different ISM conditions. We adopt the metallicity from the D16N2S2 method because it is more robust against varying ionisation parameter and the ISM pressure[27]. However, the accuracy of the D16N2S2 method might be limited by the SNR of the [SII] lines.

3.2 Metallicity: Spatial Variation The high SNR and good seeing FWHM of the MOSFIRE spectrum allows us to divide the spectrum into two independent spatial bins. The spatial apertures, labelled A1 and A2 respectively, are chosen to represent the blue-shifted and redshifted velocity components of the Hα emission line (Supplementary Fig.3). Each aperture has a diameter of $D = 1\farcs4$. The two apertures are spatially resolved, in that their centres are separated by more than the average seeing FWHM ($\sim 0\farcs8$) of the observation

The [N II]λ6583/Hα ratios for apertures A1 and A2 are identical to the global values within statistical errors (Supplementary Table 3). Using the PP04N2 method, we have $12+\log(\mathrm{O/H}) = 8.61 \pm 0.02$ for A1 and $12+\log(\mathrm{O/H}) = 8.58 \pm 0.02$ for A2, showing no significant difference. If we use the D16N2S2 calibration, we have $12+\log(\mathrm{O/H}) = 8.61 \pm 0.06$ for A1 and $12+\log(\mathrm{O/H}) = 8.83 \pm 0.06$ for A2. The component within A1 is 0.2 dex more metal-enriched than the blue component based on the D16N2S2 method, suggesting possible spatial variations in metallicity.

3.3 Electron Density The ratio of the [S II]λ6717 and [S II]λ6731 lines is a function of the electron density; the ratio decreases as the electron density increases. For example, in the very low density (n_e $<$100 cm^{-3}) environments as found in most local H II regions, the ratio of [S II]λ6717/[S II]λ6731 is $\sim$1.4; in extremely high density environments (n_e $>$10000 cm^{-3}) the ratio of [S II]λ6717/[S II]λ6731 is $\sim$0.44 [ref.[28]].

In the total aperture spectrum, both the [S II]λ6717,6731 lines are detected at a SNR of 4.6 and 4.7, respectively (Supplementary Table 3). The global electron density is therefore n_e=675^{+455}_{-255} cm^{-3} based on the relation of n_e versus [S II]λ6717/[S II]λ6731 [ref.[29]].

In aperture A1, the [S II]λ6731 line is well detected at a SNR of 12, with the [S II]λ6717 line being weaker and at a SNR $\sim$ 2. In aperture A2, the [S II]λ6731 line is not detected (SNR $<$ 1), whereas the [S II]λ6717 line is detected at a SNR $\sim$ 9. Based on the 3σ flux limit of the [S II]λ6717 line in A1 and the [S II]λ6731 line in A2, the electron density of A1 is estimated to be $n_e \gtrsim 5.7 \times 10^3$ cm^{-3} and n_e $\lesssim$ 210 cm^{-3} for A2. However, we caution that the flux limit for the [S II]λ6731 line in A2 could be contaminated by a sky line. Given the low SNR of the [S II] lines, we refrain from drawing conclusions about spatial variations in electron density. Deeper observations on [S II] lines are required to improve the accuracy of the electron density measurement and investigate the spatial distributions of n_e.

4 Systematic Uncertainties of the Total Stellar Mass

The ZFOURGE catalogue stellar mass is based on the SED fitting through the FAST fitting code (Methods). We rerun FAST using our updated aperture photometry and the spectroscopic redshift while keeping other inputs the same as the ZFOURGE catalogue; the updated stellar mass agrees with the catalogue value within 0.1 dex. Lowering the metallicity (e.g., 0.2-0.5 $Z_\odot$) does not change the stellar mass significantly (within 0.1 dex) but increases the age by a factor of $\sim$2-3.

To evaluate the robustness of M_* against different SED fitting packages, we run alternative SED-fitting codes such as `Prospector`[30] and `LE PHARE`[31]. `LE PHARE` uses a χ^2 minimisation algorithm similar to FAST, whereas `Prospector` is a new SPS modelling framework designed to account for a large number of degenerate parameters that can affect the galaxy SED[30]. `Prospector` explores the parameter space with a Bayesian MCMC approach and includes Flexible Stellar Population Synthesis models[32], variable dust attenuation, re-radiation, a nonparametric SFH and self-consistent nebular emissions[33]. With a Chabrier[34] IMF, `LE PHARE` returns a stellar mass of $\log(M_*/M_\odot)$=$10.65^{+0.08}_{-0.04}$, whereas `Prospector` returns a stellar mass of $\log(M_*/M_\odot)$=$10.84^{+0.07}_{-0.06}$ (allowing SFH to vary). We therefore conclude that the total stellar mass estimation of R5519 is $\log(M_*/M_\odot)\approx$10.8 and robust within the systematic error of 0.2 dex caused by different SED fitting methods. Applying a most extreme star formation history (10 Myr burst) will further reduce the lower limit of the stellar mass by 0.3 dex.

5 Systematic Uncertainties of Kinematic Model Fitting

We test fitting the kinematic data with only a rotation or an expansion/contraction component. We first keep V_{sys} at 0 and then test varying V_{sys} as a free parameter. For a $V_{sys} = 0$ and DOF= 2, we find that the probability of a rotation-only and expansion/contraction-only model being consistent with our data is $p = 0.07$ and $p = 0.37$, respectively (Supplementary Fig.7). For a varying V_{sys} and DOF= 1, the probability of a rotation-only and expansion/contraction-only model being consistent with our data is $p = 0.05$ and $p = 0.27$, respectively (Supplementary Fig.7). In comparison, the probability of a model with rotation and expansion/contraction (DOF= 1) is p = 0.475 (Supplementary Fig.7). We therefore conclude that a rotation and expansion/contraction model provides the best-fit to our data; a rotation-only model is the least consistent with our data, though the expansion/contraction-only model might still be viable.

We then test the assumption of our PA_0 and i by running the model fits for a range of i and PA_0 (Supplementary Fig.8). For a fixed PA_0, the magnitude of both V_{rad} and V_{rot} decreases with increasing i. For a fixed i, the magnitude of V_{rot} decreases with increasing PA_0 whereas the V_{rad} increases mildly with increasing PA_0. We have the best-fit $PA_0 = 28 \pm 10^\circ$ from the ellipse fit. For the purpose of testing the systematic uncertainty, we use $i = 29 \pm 9^\circ$ and $PA_0 = 28 \pm 10^\circ$. We randomly choose i and PA_0 from the uncertainty range above and rerun the tilted rotation+expansion/contraction ring model 500 times. The resulting 1σ scatter caused by the uncertain range of PA_0 and i for V_{rad} and V_{rot} is 71 km/s and 70 km/s. This is similar to the order of uncertainty caused by the measurement error. We note that an expansion/contraction component of our model is significant as long as the kinematic major axis is not 90° off from the photometric major axis. Deeper, high-spatial resolution IFS observations are required to reduce the systematic and measurement errors.

For the purpose of demonstrating the limitations of applying existing high-z kinematic approaches on complicated systems like R5519, we fit a simple rotating disk model to the MOSFIRE 2D Hα spectrum using the Heidelberg Emission Line Algorithm (HELA)[35,36]. Previous studies have successfully applied HELA in MOSFIRE 2D spectra to derive Hα rotation velocities[35,36]. Briefly, HELA simulates a 3D datacube of Hα lines, collapses the datacube into a MOSFIRE slit, and runs an MCMC simulation to determine the best-fit model to the observed Hα 2D spectrum. HELA assumes an arctangent rotation curve[37]

and a constant velocity dispersion, as well as an exponential profile for the radial distribution of Hα. We follow the same procedure as described extensively in a previous work[36]. We limit the inclination angle to the range of $0-35^{\circ}$. Supplementary Fig.9 shows the best-fit model from HELA. The residuals on the Hα image are significantly larger than other rotating disks at $z\sim2$ [ref.[36]]. However, because a smooth exponential 2D profile for the radial distribution of Hα is assumed in HELA, it is inconclusive if the residual comes from the deviation from a smooth Hα profile in R5519 or from an expansion component in the rotational field[38].

To test the self-consistency of our 4.4σ Hα OSIRIS detection, we use the best-fit kinematics at 5 kpc (fixing PA_0 and $PA_0 = 28^{\circ}$ and $i = 29^{\circ}$) and the NB209 Hα narrow-band image to simulate our OSIRIS observation (Supplementary Fig.4). The simulation uses the NB209 narrow-band Hα image after subtracting a small contribution from the continuum estimated from the NB119 narrow-band image. We convert the continuum subtracted NB209 flux into the Hα flux using the zero-points provided by ZFOURGE. The Hα line centroid is determined using the velocity field from the best-fit tilted rotating and expanding/contracting circular ring model; the width of the Hα line is simulated using a convolution of the instrumental width and beam-smeared with the AO-corrected spatial resolution of FWHM =0.″35. We randomly generate noises using sky spaxels from the observed datacube and run the simulated OSIRIS datacube $\sim$500 times. We are able to recover our OSIRIS Hα detection within errors (Supplementary Fig.4).

6 Collisional Time Scale

In the classic expanding wave scenario of a first ring after the collision[39–41], R_{ring}, R_{disk} (outer-edge of the disk), and n carry important information about the mass ratio (μ=$M_*{}^{intruder}/M_*{}^{host}$) and the time elapsed ($\tau_c$) after the collision. R_{ring} increases linearly with τ_c and grows faster for a larger μ. If the collision is recent ($\tau_c \lesssim 80$ Myr) or if the intruder galaxy is a dwarf (e.g., $\mu \lesssim 0.1$), R_{disk} and n remain relatively intact compared with the pre-collisional disk of the CRG host[42]. For a larger τ_c, the expanding wave redistributes the disk star and gas to larger radii, producing a larger R_{disk} and smaller n compared with the pre-collisional disk[40]. If the R_{80} we measure is the lower limit for R_{disk} of the pre-collisional disk after the collision, then the R_{80} and n of R5519 argue for a not so recent collision and a massive intruder ($\tau_c > 80$ Myr and $\mu > 0.1$).

The ratio of R_{ring} and R_{disk} provides another constraint on τ_c and μ in the context of a first expanding ring. The small ratio ($R_{ring}/R_{80} \leq 0.48$) suggests a very recent ($\tau_c < 50$ Myr for $\mu \sim 0.1$ and $\tau_c < 20$ Myr for $\mu \sim 1$) collision[40,42]. Note that $\mu \backsimeq 0.4$ if G5593 is the intruder. Indeed, the radial and rotational velocities (V_{rad}, V_{rot}) and R_{ring} of R5519 are analogous to the local CRG Arp 147 [ref.[43]] (Supplementary Fig.14), implying a similar collisional timescale[2] of $\sim$40 Myr. Here we assume a uniform expansion velocity; the derived timescale is uncertain by a factor of $\sim$2 due to the systematic and observational uncertainties of V_{rad}. This small τ_c is inconsistent with the large τ_c prompted by R_{disk} and n, and the lower limit (>50 Myr) of the stellar age on the ring.

7 The EAGLE $z\sim2$ Ring Galaxy

7.1 Identifying and Analysing the Highest-Redshift Ring Galaxy in EAGLE Simulations EAGLE is a suite of hydrodynamical simulations that follow the formation and evolution of galaxies and the growth of black holes in a cosmologically representative large box[44,45]. We exploit these simulations to study the formation and evolution of CRGs and their properties in a recent work[47].

In brief, to identify ring galaxies in EAGLE, we first classify all the galaxies in the simulations to early-types, late-types and morphologically disturbed (interacting) galaxies based on their flux radial distributions using their face-on mock *ugriz* images. In the second step, we visually inspect the morphologically disturbed galaxies and classify those that have a ring morphology. The last step is to follow the evolution history of each CRG candidate over time and see if there is any satellite(s) that collided with the ring host. Galaxies that have a ring morphology and have collided in their past with neighbouring galaxie(s) are deemed CRGs; those that have not interacted with other satellites are found to host strong bars and are similar to pseudo-rings at redshift $z = 0$.

Past observational and theoretical work suggests that in addition to the rotational velocity of the gas in these systems, CRGs have non-negligible radial velocities due to the impulse (momentum) caused by the drop-through interaction of the intruder with the disk of the ring host. As an additional check to the collisional origin of our sample, we also study the overall kinematics of the selected CRGs and find those in agreement with the analytic caustic theory[39,40,50] in which rings form from density waves. Because our previous work focuses on the entire sample of EAGLE CRGs, we do not trace the time evolution of individual CRGs at high-z.

The highest-redshift CRG identified in our simulation work[47] is at a redshift of $z = 2.23$ and is presented in Supplementary Figs.15-16. Here we analyse the kinematics of this EAGLE CRG in detail. The gravitational softening length for our simulations is 0.7 kpc at $z\sim2$, i.e., insufficient to resolve any thin/thick disk components. We use four "snipshots"[46] that have a time resolution of 60 Myr. Snipshots are snapshots stored at finer time steps. Because of the common storage limitations in supercomputers, only a small subset of the particle properties are stored in "snipshots". In EAGLE, snipshots at $z > 2$ have the fine-time resolution of $\lesssim$ 100 Myr, whereas snapshots have time resolution of few hundred Myr[46]. We define time t=0 Myr as the time when the ring feature was identified in the snapshot at $z = 2.23$, this is an arbitrarily defined time and is not representative of the exact time when the collision occurred.

In Supplementary Fig.15, we show the radius of the ring as 1D surface density peak of the star particles. We observe that the radius of the ring expands from 5, 6.5 to 15 kpc from $t = 0, 60$ Myr to 120 Myr. We tag the gas and star particles that are identified on the ring formed at $t = 0$ Myr and follow their positions in subsequent times of $t = 60, 120, 180$ Myr. The particles that make up each ring at these three timeframes are mostly composed of new particles that do not come from the ring formed at $t = 0$ Myr; this is consistent with the ring being a wave pattern.

In Supplementary Fig.16, we show the circular rotation and radial velocity of the gas particles at different radii in the $z = 2.23$ CRG for the four time sequences used in Supplementary Fig.15. We only consider the particles that lie within a radius of $r = 30$ kpc from the centre of the galaxy and assume a scale height of $h = 5$ kpc for the disk. In this case, the radial velocity is calculated for gas particles in the plane of the disk, where the plane is determined as that perpendicular to the total stellar spin vector of the galaxy. The radial velocity therefore describes the instantaneous radially outwards (positive) or inwards (negative) motion of the gas particles. Note that the instantaneous radial velocity does not reflect the motion of the density wave.

The large variations in radial velocities at all radii from $t = 0$ Myr to $t = 120$ Myr is likely triggered by the interactions with satellite galaxies as shown in Supplementary Fig.15. The ring feature is disrupted at a later snipshot ($t = 180$ Myr) due to a second passage of a satellite galaxy (Supplementary Fig.15). Hence, this ring feature has a lifespan of less than 180 Myr. This is relatively lower than the lifespan of local CRGs where the ring can expand for > 500 Myr to its maximum radius and to very low surface brightness[48]. For this EA-

GLE CRG host, there are three smaller interacting satellites with stellar masses $M_* \gtrsim 10^9\,M_\odot$. The stellar mass ratio between the intruder satellite galaxy and the ring host is ~ 0.38. The simulated CRG has a stellar mass of $M_* = 1.4\times10^{10}\,M_\odot$ and is the central galaxy within the parent halo. The total mass of the halo hosting these galaxies is $M_{200} = 1.2\times10^{12}\,M_\odot$.

7.2 Comparing the EAGLE CRG with Observations We note that this EAGLE CRG is not meant to be used as a direct comparison with R5519. Indeed, this EAGLE CRG has different physical properties from R5519. For example, in addition to being $\sim$0.23 times less massive than R5519, the SFR of the CRG is 3.8 $M_\odot$ yr^{-1}, i.e., $\sim$10 times lower than R5519. The factor of ten difference in SFR is an upper limit considering systematic effects when comparing the UV+IR SFR in observations with the EAGLE simulations[49]. The EAGLE CRG has a significant central bulge that is also absent in R5519.

Despite the differences, R5519 is found from a representative volume in the early universe that the EAGLE simulations are designed to match. It is insightful to learn from the simulated galaxy what type of environment that a $z\sim2$ CRG lives in. We see that the dynamically active environment at $z\sim2$ causes stellar and gas particles to be tugged to larger radii, resulting in a somewhat large stellar disk that is not usually seen in nearby CRGs. The simulated CRG at $t = 120$ Myr looks morphologically similar to our observed R5519, both show asymmetric clumpy features on and outside of the ring (Supplementary Fig.2 and Fig.15). Our EAGLE simulations lend an alternative explanation for the morphology of R5519: it is possible that frequent satellite interactions at high redshift have triggered a short-lived collisional ring with the outer disk representing either scattered stars from the host and satellites and/or an on-going accretion from small satellites. Finer-time resolution snapshots are required in order to make mock observations for a more quantitative comparison with observations.

Note that in the case of multiple satellite interactions before and after the formation of the first ring, the analytic estimation for τ_c from the classic expanding wave scenario[39–42] might not be directly applicable to R5519 without refinement. Therefore, the aforementioned inconsistency in τ_c is more a reflection of the inadequacy of the model used to derive it than a true inconsistency.

The snipshot at $t = 180$ Myr (Supplementary Fig.15) may look like it is beginning to form a second ring as predicted by the analytic CRG theory[50,51]. However, a later snipshot at $t = 240$ Myr (not shown in Supplementary Fig.15) reveals that the CRG is completely destroyed (including its nucleus) by the major merger at $t = 180$ Myr before a second ring can be definitively identified. This highlights the "hostile" environment typical at high redshift that can lead to the demise or short lifetime of CRGs.

8 Discussions on Alternative Origins of R5519

8.1 A gravitationally lensed arc For a scenario that R5519 is a strong gravitational lensing system, we take the radius of the ring ($0\farcs6$) as an assumed Einstein radius. We find the total mass enclosed would be $M_{\rm Ein} = 0.85-3.9\times10^{11}\,M_\odot$ for a foreground lens redshift range of $z_{lens} = 0.5-1.5$ within the $3.6-5$ kpc projected radius of the lens. Note that $M_{\rm Ein}$ increases with z_{lens}. For reference, the current highest redshift galaxy-scale lens is at $z = 1.5$ with the source at $z = 3.417$[ref.[52]]. We do not see signatures of this enclosed mass expressed in stellar light (Supplementary Fig.2), unless the foreground lens is a dwarf galaxy below the detection limit[15] ($M_* < 10^9\,M_\odot$) of ZFOURGE and with an abnormally large mass-to-light ratio. Furthermore, the persistently diffuse emission outside of the ring in multi-wavelength images is inconsistent with the morphological configuration of a gravitationally lensed arc.

8.2 A regular merger Within the caveats of our kinematic analysis, our data is consistent with a tilted rotating and expanding/contracting circular ring model. In the classical models of CRG, the ring is a radially expanding density wave. However, kinematic confirmation of the density wave is observationally challenging even for nearby galaxies. The current kinematic data alone is insufficient to rule out a regular merger.

A CRG is a special type of a major merger with a drop-through collision. Only a few percent ($\sim$ 2%) of interacting galaxies are found to be CRGs[53]. The observational difference between CRGs and other common (regular) mergers is that CRGs are geometrically simpler, characterised by a symmetric ring and a relatively well-preserved disk, whereas regular mergers are morphologically messier and retain less information about the pre-disrupted disk[39]. The prominent ring and the profile of the stellar light of R5519 is consistent with the definition of a CRG. Note that the chance of finding regular mergers projected as a symmetric ring is lower than finding a CRG[42]. Moreover, in a regular merger or tidal interaction scenario, the star formation in the central regions of galaxies contributes significantly to the total SFR whereas the star formation of a CRG usually occurs on the ring[54]. We do not detect any significant star formation activities in the central regions of the ring in R5519. We therefore think that a CRG origin is a more reasonable explanation for R5519 than a regular merger.

8.3 A secularly evolved ring By secular rings, we mean features recognised in the classifications of normal galaxies, including nuclear, inner, and outer rings[55]. In numerical simulations, such rings tend to be the product of a slow evolution of the spiral pattern due mainly to the influence of gravity torques connected to a bar or a massive oval[56]. The formation of secular rings is related to internal processes such as Lindblad resonances[55,58]. Secular rings are generally non-circular in intrinsic shape and are commonly found in barred spiral galaxies[57,58], i.e., (R)SAB in the revised Hubble classification scheme[60]. Even though in the local universe secular rings are more abundant than CRGs[55,59], the Hubble spiral sequence is not yet fully established at $z > 2$ [ref.[61]]. Most galaxies at $z > 2$ are clumpy, irregular and have small or no bulge component[62].

If R5519 is a secularly evolved ring at $z = 2.19$, we find two aspects that are challenging to explain in our current framework of disk galaxy formation and the origin of the Hubble sequence.

(1) The large disk of diffuse light outside of the ring. Although the size of the star-forming ring of R5519 is within the range of other $z\sim2$ Hα rings of secular origin[63], the extra diffuse light at large radii of R5519 is not seen in those $z\sim2$ Hα ring galaxies. From the high-resolution HST image, the diffuse disk has a rest-frame B band size of $R_{80} = 11.8$ kpc (Table 1 and Supplementary Table 4). The average outer disk size of the most massive isolated disk galaxy at $z\sim2$ is $R_{80} = 6.4$ kpc (e.g., Fig.3), a factor of 2 smaller than R5519. R5519's extended stellar disk is 1.5-2.2 times larger than the Milky Way's stellar disk[64] (Methods). Such a large extended disk of a secular origin has not been conclusively reported in observations or simulations at $z > 2$. The reason for the lack of Milky Way like large stellar disks at $z > 2$ is that it takes time to build up angular momentum to sustain such a large disk. For example, the angular momentum of the accreted gas onto halos is proportional to the cosmic time[65,66]. Recent cosmological hydrodynamical simulations show that large disks do not show up until $z\lesssim1$ [ref.[67]].

(2) The implied large ($\sim$5 kpc) bar within R5519. As secularly evolved rings are commonly found in barred spiral galaxies, the 5 kpc radius of the ring in R5519 implies a large bar of up to 5 kpc in semi-major axis. Such a large galactic bar at $z > 2$ has not been reported in simulations or observations. Barred galaxies are in general rare at $z > 2$. The fraction of spiral and barred galaxies decreases with redshift and becomes extremely difficult to find at $z > 2$ [ref.[61,68–72]]. It is true that the lack of $z > 2$ bars in observations could be caused by the limited spatial resolution and the depth of high-redshift galaxy surveys.

Bars are associated with spiral disks of the Hubble sequence and spirals are easier to observe than bars. Many high-redshift observations have pointed out that spiral galaxies themselves do not fully emerge until $z < 2$ [ref.[61,71]]. For example, there are less than three galaxies that are observationally confirmed to be spiral galaxies at $z > 2$[70,72] and no conclusive barred spirals have been observationally confirmed at $z > 2$ [ref.[69,73]].

Cosmological hydrodynamical simulations show that the dynamically active environment at $z > 1$ is hostile to bar formation[68,69]. In one of our recent work[73], we investigate the formation of a barred spiral at $z \sim 2$ in zoom-in cosmological hydrodynamical simulations. We find that such a rare barred spiral galaxy (R_{80} ~2.5 times smaller and bar size ~7 times smaller than R5519) is found in a relatively isolated environment without companions. Our finding is consistent with previous studies that bar formation at high redshift is difficult because any merger or violent gas accretion event would have destroyed the bar[68,69]. This picture is also consistent with the overall evolution of the Hubble sequence with respect to the evolution of the environment[74,75]. If we interpret R5519 as one of the outliers that formed a bar in the early universe, then the active group environment it resides in is counterintuitive to findings in simulations. A collisional ring origin, on the other hand, can naturally account for the large diffuse disk and does not require the existence of a large bar in R5519.

Note that non-circular orbits and projection effects can mimic the impression of an expanding/contracting component in the velocity field. Modelling of non-circular orbits requires a deeper and more spatially resolved 2D kinematic map than our current data. However, the projected velocity[76] of non-circular velocity is usually much lower than the expansion/contracting velocity of CRGs. Most nearby CRGs have large (~50-200 km/s) expansion velocities[43,77,78]. The large $V_{rad,5kpc}$ = 226 ± 90 km/s we derive for R5519 is inconsistent with a secular ring and more consistent with a collisional ring (e.g., $V_{rad,5.8kpc}$ = 225 ± 8 km/s for Apr 147 [ref.[43]]).

Finally, a remark on using kinematics to distinguish a CRG from a regular merger and an isolated disk. In the post-collisional disk of a CRG, the departure of the 2D kinematic field from an isolated pure rotational disk is a function of the time elapsed from the collision[54]. We caution that very deep IFS observations and careful modelling are required to distinguish the 2D kinematic field from a post-collisional CRG disk, an isolated rotation-only disk, and a rotation-only disk that is being tidally perturbed. Our preferred interpretation of R5519 being a CRG is based on a combined evidence of kinematical, environmental, and photometric analysis. We urge follow-up observations to further verify/falsify our interpretations.

9 The Implied Number Density of CRG at $z \sim 2$

The co-moving volume of our observation is 1.1×10^6 cMpc^3 based on the survey area of the ZFOURGE COSMOS field (11×11 arcmin^2) and the redshift range ($z_p = 1.8 - 2.5$). The EAGLE simulations[47] cover a similar co-moving volume of $(100)^3$ cMpc^3. Both our observation and the EAGLE simulations find only one collisional ring galaxy candidate at $z > 1.8$, implying a co-moving volume density (n_c) of $\sim9\times10^{-7}$ cMpc^{-3} or a volume number density rate of $\sim2\times10^{-6}$ cMpc^{-3} Gyr^{-1} at $z \sim 2$.

We consider the following selection effects that can affect the observed volume number density n_c estimated above.

(1) The ZFOURGE survey is complete[14] to stellar mass $M_* > 10^{9.5}M_\odot$ at $z \sim 2$ and our morphological identification is robust to galaxies that have $R_{80} \gtrsim 4$ kpc. Our estimation of n_c will miss CRGs of small ring sizes or low-mass hosts. However, assuming that the ring size distribution of CRGs does not evolve with redshift, the missing fraction of small rings are ~10%. For example, the median ring radius of local CRGs is 15-20 kpc and less than ~12% of local CRGs have ring radius less than 4 kpc[53].

(2) We use the 3D-HST F160W band image for morphological identifications. The 5σ limiting magnitude[14] of the F160W image is 26.4 mag. Rings with surface brightness lower than this detection limit will be missed in our search.

To demonstrate this effect, we simulate what Arp 147 and the Cartwheel galaxy would look like at $z = 2.19$ in the HST F160W band for our current observational depth. Our simulation follows the standard red-shifting methodology[79] that considers the cosmological angular size evolution, surface brightness dimming and K-correction. We do not apply any intrinsic evolution in galaxy sizes. We then resample and convolve the redshifted images to match the HST F160W pixel size and PSF. We use B band images at $z \sim 0$ for the simulation to minimise the K-correction (HST F160W corresponds to rest-frame B/V band at $z \approx 2$). The B-band images are taken from the local CRG sample[42] for Arp 147 and the HST archive for the Cartwheel.

The simulated images of Arp 147 and the Cartwheel are shown in Supplementary Fig.14. For comparison, the observed image of R5519 in the same F160W band are zoomed-in to match the same field of view as the simulated images. By simply placing Arp 147 and the Cartwheel at $z = 2.19$, neither of them would be detected in our observations. However, if we manually increase the intrinsic rest-frame B-band luminosity (L_B) by a similar factor (~4-8) as the increased SFR of R5519 at $z \sim 2$, the average surface brightness of both systems will be above a 5σ detection limit.

Note that the Σ_{SFR} of R5519 is ~4 times higher than Arp 147, ~ 8 times higher than the first ring of the Cartwheel and ~50 times brighter than the secondary ring of Cartwheel. Our assumed intrinsic luminosity evolution of CRGs in the simulations is consistent with $z \sim$ 2 SF galaxies having a higher SFR (and thus being brighter in the rest-frame B band) than local galaxies. For example, based on the empirical relation between SFR and L_B[80,81], a $4-8$ times rise in SFR corresponds to an increase of ~3-5 in L_B.

Combining the constraints of (1) and (2), and based on the mass-size relation at $z \sim 2$ [ref.[82]], we find that a total F160W magnitude of brighter than 23.9 will allow galaxies to have sufficient number of bright pixels (equivalent to an area of $R_{80} \gtrsim 4$ kpc) to be detected above the 5σ limiting magnitude. Assuming that CRG hosts at $z \sim 2$ are within the 2σ scatter of the SFR-M_* "main-sequence" relation, and based on the empirical relation between the B-band luminosity and SFR[80,81], we estimate that our observation is complete for $z \sim 2$ SF galaxies of stellar masses $\gtrsim 10^{10}M_\odot$. Note that the EAGLE ring simulations[47] also select galaxies of $M_* \gtrsim 10^{10}M_\odot$ at $z \sim 2$.

Both our observation and the EAGLE simulations yield a similar co-moving volume density of $n_c \sim 9\times10^{-7}$ cMpc^{-3} for CRGs that are massive ($M_* \gtrsim 10^{10}M_\odot$) and reside within the 2σ scatter of the SFR-M_* relation at $z \sim 2$. Our estimated n_c does not account for galaxies that are 2σ below the "main-sequence" relation at $z \sim 2$. However, those low SFR galaxies are $\gtrsim 100$ rarer than "main-sequence" SF galaxies at at $z \sim 2$ [ref.[83]] and are unlikely to contribute significantly to our estimated n_c.

We do note that our observations will miss low-mass ($M_* \lesssim 10^{10}M_\odot$) galaxies at $z \sim 2$. Our observed number density of massive CRGs at $z \sim 2$ is a factor of ~ 140 less than what is expected from the previous $(1+z)^{4.5}$ scaling relation with the cosmic merger rate[85]. Using a more recent cosmic merger rate scaling relation $(1+z)^{2.2-2.5}$ for high-mass ($M_* \geq 10^{10}M_\odot$) only galaxies[84], the expectation for massive CRG number density is still a factor of 11-15 larger at $z \sim 2$ than at $z \sim 0$.

Finally, we estimate that the cosmic variance could contribute to an additional 10-20% uncertainty in our observed number density[86,87].

10 Possible Explanation for the Number Density Evolution of CRGs with Redshift

We emphasise that our conclusion on the small number density of CRGs at $z \sim 2$ is confined to relatively massive ($M_* \geq 10^{10} M_\odot$) galaxy hosts (Method, Section 8). It is possible that there are more CRGs at high redshift that are below current observational limits. Large expansion velocities will cause collisional rings to be short-lived and therefore difficult to observe. However, it is unknown if our measured expansion velocity of R5519 is typical of other CRGs at high redshift. We speculate two other factors that could lead to the rarity of large collisional rings at high redshift ($z \gtrsim 2$).

Local CRGs are often found in loose groups instead of compact groups or galaxy clusters[53]. Even though interaction rates are higher in dense environments (e.g., clusters), the high velocity dispersions between cluster members and fly-by interactions can easily destroy the ring features. The galaxy environment at high redshift is similarly very active because of the frequent interactions with satellites and high gas accretion rates[74,84]. Our $z = 2.23$ EAGLE simulated ring is short-lived ($\sim$200 Myr before it is completely destroyed by another merger) in this dynamically chaotic high-redshift environment (Supplementary Fig.15). The short lifetime of the ring could make CRGs appear rare in observations even though the required collisions happen frequently. Recent cosmological simulations imply that local-like galaxy groups do not fully emerge until $z \lesssim 2$ [ref.[88]]. Observing the number density of CRGs across cosmic time could therefore provide an alternative constraint on the assembly and evolution of local-like galaxy groups.

Another factor that could make large CRGs hard to find at high redshift is related to the properties of the pre-collisional disk. Most models of nearby collisional ring galaxies assume that the target galaxy has a large thin stellar disk, i.e., the vertical disk scale length is about 1/10 of the radial scale length[40,41,89,90]. This assumption is valid for most spiral galaxies in the local universe. However, the vertical disk length of $z \sim 2$ galaxies can be a factor of $\sim$8 larger[91], as reflected by their high velocity dispersions[63,92].

Collisional rings and spiral arms share a close connection in the origin of their structures. Both are considered as a part of the stellar dynamical orbit crowding process in response to a perturbation gravity force[39,93,94]. The epicyclic oscillations of perturbed stellar orbits drive propagating density waves that are sustainable in large thin disks. However, a heated vertical disk can cause spiral and ring waves to rapidly die out[95,96]. We speculate that the lack of large spiral galaxies and collisional rings might both be related to the late formation time of thin disks. A large thin disk needs high angular momentum to be stable[67]. Cosmological simulations show that massive ($M_* \geq 10^{10} M_\odot$) galaxies commence the development of their disks between $1 < z < 2$ and large, stable disks are established at only at $z \lesssim 1$ [ref.[67,97]]. Galactic Archeology also shows that the thin disk of our Milky Way did not form until $z \sim 1$ [ref.[98]].

Finding the onset of large spiral galaxies remains a major problem in galaxy formation[61] and is one of the keys to unlock the origin of the Hubble sequence[74]. Given the different structure of high-redshift disk galaxies (smaller sizes, more turbulent ISM, more chaotic morphology and larger disk height), it becomes challenging to visually separate spiral arms from clumpy, irregular disks at high redshift. For this reason, the earliest formation epoch of spiral galaxies is poorly constrained in theories and observations[70,72,74,99]. Large ring galaxies, while rare, are relatively easy to identify and follow up in detail, thus providing a unique diagnostic to constrain the onset of thin disks and spiral galaxies.

Additional Acknowledgements

T.Y. and C.L. acknowledge the support of an ASTRO 3D Fellowship. GGK acknowledges the support of the Australian Research Council through the Discovery Project DP170103470. K. Tran and L. Alcorn acknowledge support by the USA National Science Foundation under Grant Number 1410728. CMSS acknowledges funding through the H2020 ERC Consolidator Grant 683184. T.Y. thanks for useful discussions with L. Hernquist, J. Bland-Hawthorn, E. Wisnioski, T. Mendel, A. Graham, M. Arabsalmani, and S. Leslie.

Part of the data presented herein were obtained at the W. M. Keck Observatory, which is operated as a scientific partnership among the California Institute of Technology, the University of California and the National Aeronautics and Space Administration. The Observatory was made possible by the generous financial support of the W. M. Keck Foundation. The authors wish to recognise and acknowledge the very significant cultural role and reverence that the summit of Mauna Kea has always had within the indigenous Hawaiian community. We are most fortunate to have the opportunity to conduct observations from this mountain.

References

1. McLean, I. S. *et al.* MOSFIRE, the multi-object spectrometer for infrared exploration at the Keck Observatory. *(SPIE) Conference Series* **8446**, (2012).
2. Nanayakkara, T. *et al.* ZFIRE: A KECK/MOSFIRE Spectroscopic Survey of Galaxies in Rich Environments at $z \sim 2$. *Astrophys. J.* **828**, 21 (2016).
3. Allen, R. J. *et al.* The Size Evolution of Star-forming Galaxies since $z \sim 7$ Using ZFOURGE. *Astrophys. J.* **834**, L11 (2017).
4. Larkin, J. *et al.* OSIRIS: A diffraction limited integral field spectrograph for Keck. *New Astronomy Reviews* **50**, 362–364 (2006).
5. Wizinowich, P. L. *et al.* The W. M. Keck Observatory Laser Guide Star Adaptive Optics System: Overview. *PASP* **118**, 297–309 (2006).
6. Skelton, R. E. *et al.* 3D-HST WFC3-selected Photometric Catalogs in the Five CANDELS/3D-HST Fields: Photometry, Photometric Redshifts, and Stellar Masses. *Astrophys. J. Supp.* **214**, 24 (2014).
7. Grogin, N. A. *et al.* CANDELS: The Cosmic Assembly Near-infrared Deep Extragalactic Legacy Survey. *Astrophys. J. Supp.* **197**, 35 (2011).
8. Koekemoer, A. M. *et al.* CANDELS: The Cosmic Assembly Near-infrared Deep Extragalactic Legacy Survey −The Hubble Space Telescope Observations, Imaging Data Products, and Mosaics. *Astrophys. J. Supp.* **197**, 36 (2011).
9. Davies, R. I. A method to remove residual OH emission from near-infrared spectra. *Mon. Not. R. Astron. Soc.* **375**, 1099–1105 (2007).
10. Rousselot, P. *et al.* Night-sky spectral atlas of OH emission lines in the near-infrared. *Astron. Astrophys.* **354**, 1134–1150 (2000).
11. Scoville, N. *et al.* The Cosmic Evolution Survey (COSMOS): Overview. *Astrophys. J. Supp.* **172**, 1–8 (2007).
12. Persson, S. E. *et al.* FourStar: The Near-Infrared Imager for the 6.5m Baade Telescope at Las Campanas Observatory. *PASP* **125**, 654–682 (2013).
13. Papovich, C. *et al.* ZFOURGE/CANDELS: On the Evolution of M* Galaxy Progenitors from $z = 3$ to 0.5. *Astrophys. J.* **803**, 26 (2015).
14. Straatman, C. M. *et al.* The FourStar Galaxy Evolution Survey (ZFOURGE): Ultraviolet to Far-infrared Catalogs, Medium-bandwidth Photometric Redshifts with Improved Accuracy, Stellar Masses, and Confirmation of Quiescent Galaxies to $z \sim 3.5$. *Astrophys. J.* **830**, 51 (2016).
15. Tomczak, A. R. *et al.* The SFR-M* Relation and Empirical Star-Formation Histories from ZFOURGE at $0.5 < z < 4$. *Astrophys. J.* **817**, 118 (2016).
16. Cowley, M. J. *et al.* ZFOURGE catalogue of AGN candidates: an enhancement of 160-μm-derived star formation rates in active galaxies to $z = 3.2$. *Mon. Not. R. Astron. Soc.* **457**, 629–641 (2016).
17. Forrest, B. *et al.* ZFOURGE: Using Composite Spectral Energy Distributions to Characterize Galaxy Populations at $1 < z < 4$. *Astrophys. J.* **863**, 131 (2018).
18. Labbe, I. *et al.* Spitzer IRAC Confirmation of z850-Dropout Galaxies in the Hubble Ultra Deep Field: Stellar Masses and Ages at $z \sim 7$. *Astrophys. J.* **649**, L67-L70 (2006).
19. Pettini, M.,Pagel, B. E. J. [OIII]/[NII] as an abundance indicator at high redshift. *Mon. Not. R. Astron. Soc.* **348**, L59–L63 (2004).
20. Yuan, T. Kewley, L. J. Swinbank, A. M. & Richard, J. The A2667 Giant Arc at $z = 1.03$: Evidence for Large-Scale Shocks at High Redshift. *Astrophys. J.* **759**, 66 (2012).

21. Kewley, L. J. *et al.* Theoretical Evolution of Optical Strong Lines across Cosmic Time. *Astrophys. J.* **774**, 100 (2013).
22. Dopita, M. A. Kewley, L. J. Sutherland, R. S. & Nicholls, D. C. Chemical abundances in high-redshift galaxies: a powerful new emission line diagnostic. *Ap&SS* **361**, 61 (2016).
23. Erb, D. K. *et al.* The Mass-Metallicity Relation at $z > 2$. *Astrophys. J.* **644**, 813–828 (2006).
24. Sanders, R. L. *et al.* The MOSDEF Survey: Mass, Metallicity, and Star-formation Rate at $z \sim 2.3$. *Astrophys. J.* **799**, 138 (2015).
25. Kacprzak, G. G. *et al.* The Absence of an Environmental Dependence in the Mass—Metallicity Relation at $z \sim 2$. *Astrophys. J.* **802**, L26 (2015).
26. D'Eugenio, F. *et al.* The gas-phase metallicities of star-forming galaxies in aperture-matched SDSS samples follow potential rather than mass or average surface density. *Mon. Not. R. Astron. Soc.* **479**, 1807–1821 (2018).
27. Cameron, A. *et al.* Prospects for Extending the Mass-Metallicity Relation to Low Mass at High Redshift: A Case Study at $z \sim 1$. *Astrophys. J.* **882**, 116 (2019).
28. Osterbrock, D. E. & Ferland, G. J. Astrophysics of gaseous nebulae and active galactic nuclei. *Astrophysics of gaseous nebulae and active galactic nuclei, 2nd. ed., CA: University Science Books* (2006).
29. Proxauf, B. ttl, S. & Kimeswenger, S. Upgrading electron temperature and electron density diagnostic diagrams of forbidden line emission. *Astron. Astrophys.* **561**, A10 (2014).
30. Leja, J. *et al.* Deriving Physical Properties from Broadband Photometry with `Prospector`: Description of the Model and a Demonstration of its Accuracy Using 129 Galaxies in the Local Universe. *Astrophys. J.* **837**, 170 (2017).
31. Ilbert, O. *et al.* Galaxy Stellar Mass Assembly Between $0.2 < z < 2$ from the S-COSMOS Survey. *Astrophys. J.* **709**, 644–663 (2010).
32. Conroy, C.,Gunn, J. E. & White, M. The Propagation of Uncertainties in Stellar Population Synthesis Modeling. I. The Relevance of Uncertain Aspects of Stellar Evolution and the Initial Mass Function to the Derived Physical Properties of Galaxies. *Astrophys. J.* **699**, 486–506 (2009).
33. Byler, N. *et al.* Nebular Continuum and Line Emission in Stellar Population Synthesis Models. *Astrophys. J.* **840**, 44 (2017).
34. Chabrier, G. Galactic Stellar and Substellar Initial Mass Function. *PASP* **115**, 763–795 (2003).
35. Straatman, C. M. S. *et al.* ZFIRE: The Evolution of the Stellar Mass Tully-Fisher Relation to Redshift $\sim$2.2 *Astrophys. J.* **839**, 57 (2017).
36. Alcorn, L. Y. *et al.* ZFIRE: 3D Modeling of Rotation, Dispersion, and Angular Momentum of Star-forming Galaxies at $z \sim 2$. *Astrophys. J.* **858**, 47 (2018).
37. Courteau, S. Optical Rotation Curves and Line widths for Tully-Fisher Applications. *Astron. J.* **114**, 2402 (1997).
38. Higdon, J. L. Higdon, S. J. U. & Rand, R. J. Wheels of Fire. IV. Star Formation and the Neutral Interstellar Medium in the Ring Galaxy AM0644-741. *Astrophys. J.* **739**, 97 (2011).
39. Appleton, P. N., Struck-Marcell, C. Collisional Ring Galaxies. *FCPh* **16**, 111–220 (1996).
40. Gerber, R. A., Lamb, S. A. & Balsara, D. S. A stellar and gas dynamical numerical model of ring galaxies. *Mon. Not. R. Astron. Soc.* **278**, 345–366 (1996).
41. Mapelli, M. & Mayer, L. Ring galaxies from off-centre collisions. *Mon. Not. R. Astron. Soc.* **420**, 1158–1166 (2012).
42. Romano, R., Mayya, Y. D. & Vorobyov, E. I. Stellar Disks of Collisional Ring Galaxies. I. New Multiband Images, Radial Intensity and Color Profiles, and Confrontation with N-Body Simulations. *Astron. J.* **136**, 1259–1289 (2008).
43. Fogarty, L. *et al.* SWIFT observations of the Arp 147 ring galaxy system. *Mon. Not. R. Astron. Soc.* **417**, 853–844 (2011).
44. Schaye, J. *et al.* The EAGLE project: simulating the evolution and assembly of galaxies and their environments. *Mon. Not. R. Astron. Soc.* **446**, 521–554 (2015).
45. Crain, R. A. *et al.* The EAGLE simulations of galaxy formation: calibration of subgrid physics and model variations. *Mon. Not. R. Astron. Soc.* **450**, 1937–1961 (2015).
46. Crain, R. A. *et al.* The EAGLE simulations: atomic hydrogen associated with galaxies. *Mon. Not. R. Astron. Soc.* **464**, 4204–4226 (2017).
47. Elagali, A. *et al.* Ring galaxies in the EAGLE hydrodynamical simulations. *Mon. Not. R. Astron. Soc.* **481**, 2951–2969 (2018).
48. Mapelli, M. *et al.* Are ring galaxies the ancestors of giant low surface brightness galaxies? *Mon. Not. R. Astron. Soc.* **383**, 1223–1231 (2008).
49. Katsianis, A. *et al.* The high-redshift SFR-M* relation is sensitive to the employed star formation rate and stellar mass indicators: towards addressing the tension between observations and simulations. *Mon. Not. R. Astron. Soc.* **492**, 5592–5606 (2020).
50. Struck, C. Applying the analytic theory of colliding ring galaxies. *Mon. Not. R. Astron. Soc.* **403**, 1516-1530 (2010).
51. Smith, R. *et al.* Numerical modelling of Auriga's Wheel - a new ring galaxy. *Mon. Not. R. Astron. Soc.* **423**, 543–557 (2012).
52. van der Wel, A.*et al.* Discovery of a Quadruple Lens in CANDELS with a Record Lens Redshift $z = 1.53$. *Astrophys. J.* **777**, L17 (2013).
53. Madore, B. F., Nelson, E. & Petrillo, K. Atlas and Catalog of Collisional Ring Galaxies. *Astrophys. J. Supp.* **181**, 572–604 (2009).
54. Arabsalmani, M. *et al.* The host galaxy of GRB 980425/SN1998bw: a collisional ring galaxy. *Mon. Not. R. Astron. Soc.* **485**, 5411–5422 (2019).
55. Buta, R. J. & Combes, F. Galactic Rings. *Fund. Cosmic Phys.* **17**, 95–281 (1996).
56. Schwarz, M. P. The response of gas in a galactic disk to bar forcing. *Astrophys. J.* **247**, 77–88 (1981).
57. Buta, R. J. Resonance Rings and Galaxy Morphology. *Ap&SS* **269**, 79–99 (1999).
58. Buta, R. J. Galactic rings revisited - I. CVRHS classifications of 3962 ringed galaxies from the Galaxy Zoo 2. *Mon. Not. R. Astron. Soc.* **471**, 4027–4046 (2017).
59. Theys, J. C. & Spiegel, E. A. Ring Galaxies. I. *Astrophys. J.* **208**, 650–661 (1976).
60. de Vaucouleurs, G. Classification and Morphology of External Galaxies. *Handbuch der Physik* **53**, 275 (1959).
61. Conselice, C. J. The Evolution of Galaxy Structure Over Cosmic Time. *ARA&A* **52**, 291–337 (2014).
62. Bournaud, F. & Elmegreen, B. G. Unstable Disks at High Redshift: Evidence for Smooth Accretion in Galaxy Formation. *Astrophys. J.* **694**, L158–L161 (2009).
63. Genzel, R. *et al.* From Rings to Bulges: Evidence for Rapid Secular Galaxy Evolution at $z \sim 2$ from Integral Field Spectroscopy in the SINS Survey. *Astrophys. J.* **687**, 59–77 (2008).
64. van der Kruit, P. C. & Freeman, K. C. Galaxy Disks. *ARA&A* **49**, 301–371 (2011).
65. Catelan, P. & Theuns, T. Evolution of the angular momentum of proto-galaxies from tidal torques: Zel'dovich approximation. *Mon. Not. R. Astron. Soc.* **282**, 436–454 (1996).
66. Catelan, P. & Theuns, T. Non-linear evolution of the angular momentum of proto-structures from tidal torques. *Mon. Not. R. Astron. Soc.* **282**, 455–469 (1996).
67. Lagos, C. d. P. *et al.* Angular momentum evolution of galaxies in EAGLE. *Mon. Not. R. Astron. Soc.* **464**, 3850–3870 (2017).
68. Sheth, K. *et al.* Hot Disks and Delayed Bar Formation. *Astrophys. J.* **758**, 136 (2012).
69. Kraljic, F., Bournaud, F. & Martig, M. The Two-phase Formation History of Spiral Galaxies Traced by the Cosmic Evolution of the Bar Fraction. *Astrophys. J.* **757**, 60 (2012).
70. Law, D. R. *et al.* High velocity dispersion in a rare grand-design spiral galaxy at redshift $z = 2.18$. *Nature* **487**, 338–340 (2012).
71. Elmegreen, D. M. & Elmegreen, B. G. The Onset of Spiral Structure in the Universe. *Astrophys. J.* **781**, 11 (2014).
72. Yuan, T.-T. *et al.* The Most Ancient Spiral Galaxy: A 2.6-Gyr-old Disk with a Tranquil Velocity Field. *Astrophys. J.* **850**, 61 (2017).
73. Vincenzo, F., Kobayashi, C. & Yuan, T. Zoom-in cosmological hydrodynamical simulation of a star-forming barred, spiral galaxy at redshift $z = 2$. *Mon. Not. R. Astron. Soc.* **488**, 4674-4689 (2019).
74. Cen, R. Evolution of Cold Streams and the Emergence of the Hubble Sequence. *Astrophys. J.* **789**, L21 (2014).
75. Cen, R. On the Origin of the Hubble Sequence: I. Insights on Galaxy Color Migration from Cosmological Simulations. *Astrophys. J.* **781**, 38 (2014).
76. Kormendy, J. & Kennicutt, Jr., R. C. Secular Evolution and the Formation of Pseudobulges in Disk Galaxies. *ARA&A* **42**, 603–683 (2004).
77. Few, M. A., Madore, B. F. & Arp, H. C. Ring galaxies. I - Kinematics of the southern ring galaxy AM 064-741. *Mon. Not. R. Astron. Soc.* **199**, 633–647 (1982).
78. Higdon, J. L., Higdon, S. J. U., Martín Ruiz, S. & Rand, R. J. Molecular Gas and Star Formation in the Cartwheel. *Astrophys. J.* **814**, L1 (2015).
79. Giavalisco, M. *et al.* On the Morphology of the HST Faint Galaxies. *Astron. J.* **112**, 369 (1996).
80. Salim, S. *et al.* Mid-IR Luminosities and UV/Optical Star Formation Rates at $z < 1.4$. *Astrophys. J.* **700**, 161–182 (2009).
81. Mostek, N. *et al.* Calibrating the Star Formation Rate at $z \sim 1$ from Optical Data. *Astrophys. J.* **746**, 124 (2012).
82. Allen, R. J. *et al.* The Differential Size Growth of Field and Cluster Galaxies at $z = 2.1$ Using the ZFOURGE Survey. *Astrophys. J.* **806**, 3 (2015).
83. Rodighiero, G. *et al.* The Lesser Role of Starbursts in Star Formation at $z = 2$. *Astrophys. J.* **739**, L40 (2011).

84. Rodriguez-Gomez, V. *et al.* The merger rate of galaxies in the Illustris simulation: a comparison with observations and semi-empirical models. *Mon. Not. R. Astron. Soc.* **449**, 49–64 (2015).
85. Lavery, R. J., Remijan, A., Charmandaris, V., Hayes, R. D. & Ring, A. A. Probing the Evolution of the Galaxy Interaction/Merger Rate Using Collisional Ring Galaxies. *Astrophys. J.* **612**, 679–689 (2004).
86. Trenti, M. & Stiavelli, M. Cosmic Variance and Its Effect on the Luminosity Function Determination in Deep High-z Surveys. *Astrophys. J.* **676**, 767–780 (2008).
87. Moster, B. P. *et al.* A Cosmic Variance Cookbook. *Astrophys. J.* **731**, 113 (2011).
88. Gupta, A. *et al.* Chemical pre-processing of cluster galaxies over the past 10 billion years in the IllustrisTNG simulations. *Mon. Not. R. Astron. Soc.* **477**, L35 (2018).
89. Fiacconi, D. *et al.* Adaptive mesh refinement simulations of collisional ring galaxies: effects of the interaction geometry. *Mon. Not. R. Astron. Soc.* **425**, 2255–2266 (2012).
90. Renaud, F. *et al.* Morphology and enhanced star formation in a Cartwheel-like ring galaxy. *Mon. Not. R. Astron. Soc.* **473**, 585–602 (2018).
91. Glazebrook, K. The Dawes Review 1: Kinematic Studies of Star-Forming Galaxies Across Cosmic Time. *Publications of the Astronomical Society of Australia* **30**, 056 (2013).
92. Wisnioski, E. *et al.* The KMOS^{3D} Survey: Design, First Results, and the Evolution of Galaxy Kinematics from $0.7 \leq z \leq 2.7$. *Astrophys. J.* **799**, 209 (2015).
93. Julian, W. H. & Toomre, A. Non-Axisymmetric Responses of Differentially Rotating Disks of Stars. *Mon. Not. R. Astron. Soc.* **146**, 810 (1966).
94. Hernquist, L. & Weil, M. L. Spokes in Ring Galaxies. *Mon. Not. R. Astron. Soc.* **261**, 804 (1993).
95. Bertin, G. & Lin, C. C. Spiral structure in galaxies a density wave theory. *Cambridge, MA: MIT Press* ISBN0262023962 (1996).
96. Elmegreen, B. G. & Thomasson, M. Grand Design and Flocculent Spiral Structure in Computer Simulations with Star Formation and Gas Heating. *Astron. Astrophys.* **272**, 37 (1993).
97. Park, M. J. *et al.* New Horizon: On the Origin of the Stellar Disk and Spheroid of Field Galaxies at $z = 0.7$. *Astrophys. J.* **883**, 25 (2019).
98. Freeman, K. & Bland-Hawthorn, J. The New Galaxy: Signatures of Its Formation. *ARA&A* **40**, 487–537 (2002).
99. Hodge, J.-A. *et al.* ALMA reveals evidence for spiral arms, bars, and rings in high-redshift submillimeter galaxies. *Astrophys. J.* **876**, 130 (2019).
100. van der Wel , A. *et al.* 3D-HST+CANDELS: The Evolution of the Galaxy Size-Mass Distribution since $z = 3$. *Astrophys. J.* **788**, 28 (2014).
101. Salim, S. *et al.* UV Star Formation Rates in the Local Universe. *Astrophys. J. Supp.* **173**, 267–292 (2007).
102. Pearson, W. J. *et al.* Main sequence of star forming galaxies beyond the Herschel confusion limit. *Astron. Astrophys.* **615**, A146 (2018).
103. Higdon, J. L. Wheels of Fire. I. Massive Star Formation in the Cartwheel Ring Galaxy. *Astrophys. J.* **455**, 524 (1995).
104. Crivellari09, E. ,Wolter, A. & Trinchieri, G. The Cartwheel galaxy with XMM-Newton. *Astron. Astrophys.* **501**, 445–453 (2009).
105. Licquia, T. C. & Newman, J. A. Improved Estimates of the Milky Way's Stellar Mass and Star Formation Rate from Hierarchical Bayesian Meta-Analysis. *Astrophys. J.* **806**, 96 (2015).

SUPPLEMENTARY FIGURES AND TABLES

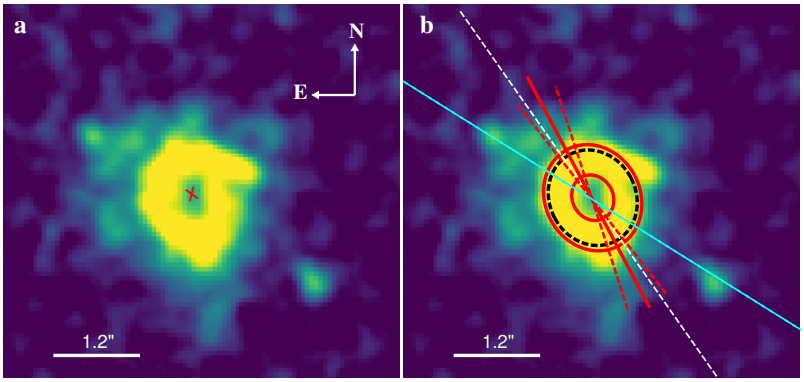

Supplementary Figure 1 – Fitting ellipses to the ring structure in high-resolution HST images. **a,** we use the combined F125W+F140W+F160W HST images from CANDELS[6,7] to quantify the size of the ring. The red cross shows the initial centre of the ring before the fitting. The image is smoothed by three pixels to increase the signal-to-noise ratio. **b,** the red ellipses show the best-fit double ellipse model, with the red solid and red dashed lines denoting the best-fit position angle (PA) and 1σ errors of the model. The black ellipse shows the best-fit single ellipse model. The cyan dashed line shows the PA of the MOSFIRE slit. For reference, the white dashed line shows the literature PA from the 3D-HST catalogue based on the Sersic profile model fit to the image[100]. A scale of $1\farcs2$ ($\sim$10 kpc) is shown. The details of the ellipse fit procedure are described in Methods.

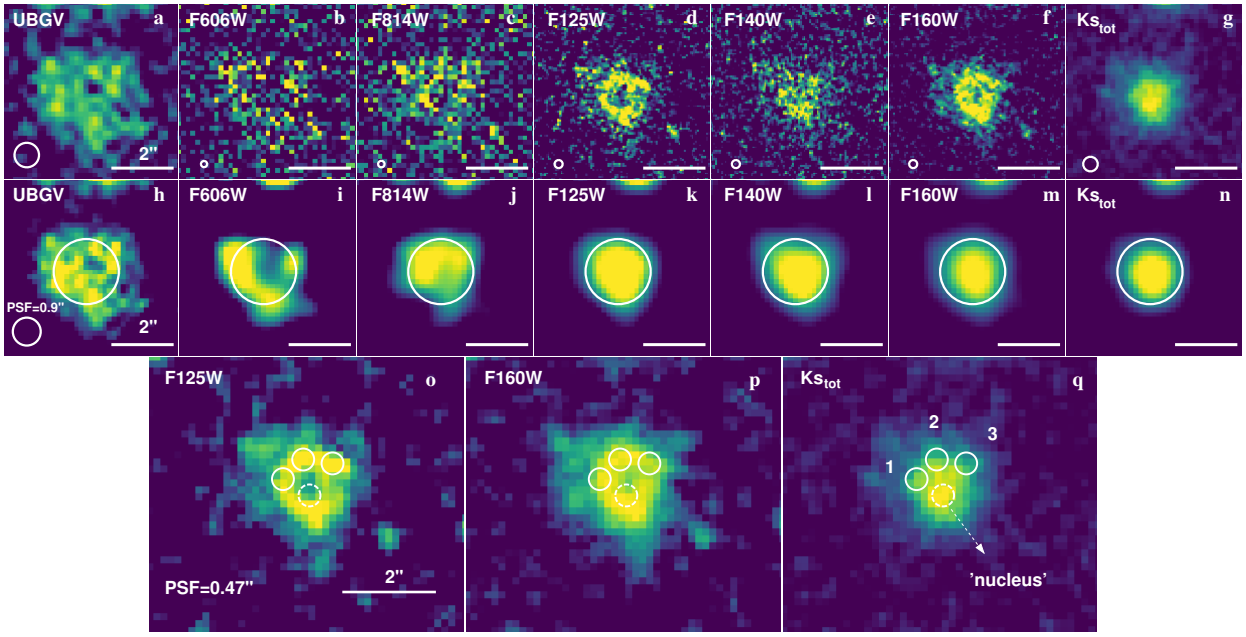

Supplementary Figure 2 – Multi-wavelength morphology of R5519. The images are selected from the ZFOURGE catalogue. North is up and East is to the left. A scale of $2\farcs0$ ($\sim$17 kpc) is shown as a horizontal bar on each image. All images have a pixel scale of $0\farcs15$, except for the HST F125W, F140W, and F160W images in the first row, where we show the original 3D-HST CANDELS[6,7] images with a pixel scale of $0\farcs06$. **a-g,** the original images selected from the ZFOURGE catalogue. The UBGV stacked image represents the ground-based image in the shortest wavelength. The HST images (F606W, F814W, F125W, F140W, and F160W) cover both the optical and the near-IR wavelengths. The Ks_{tot} band image represents the ground-based image in the longest wavelength. The PSF of each image is marked as an empty white circle at the bottom left. **h-n,**same as the top row, but showing the ZFOURGE PSF convolved images; the images are convolved with a Moffat profile to match the largest PSF (FWHM $\sim 0\farcs9$) of the ground-based images. The solid white circles indicate a diameter of $2\farcs1$ used for the global aperture photometry. **o-q,** PSF matched HST F125W, F160W, and ZFOURGE Ks_{tot} band images. The white circles show the apertures used to compare the colours of the postulated "nucleus" (dashed circle) with three regions on the ring (solid circles) (Method). The aperture has a diameter of $0\farcs47$, equivalent to the PSF of the convolved images.

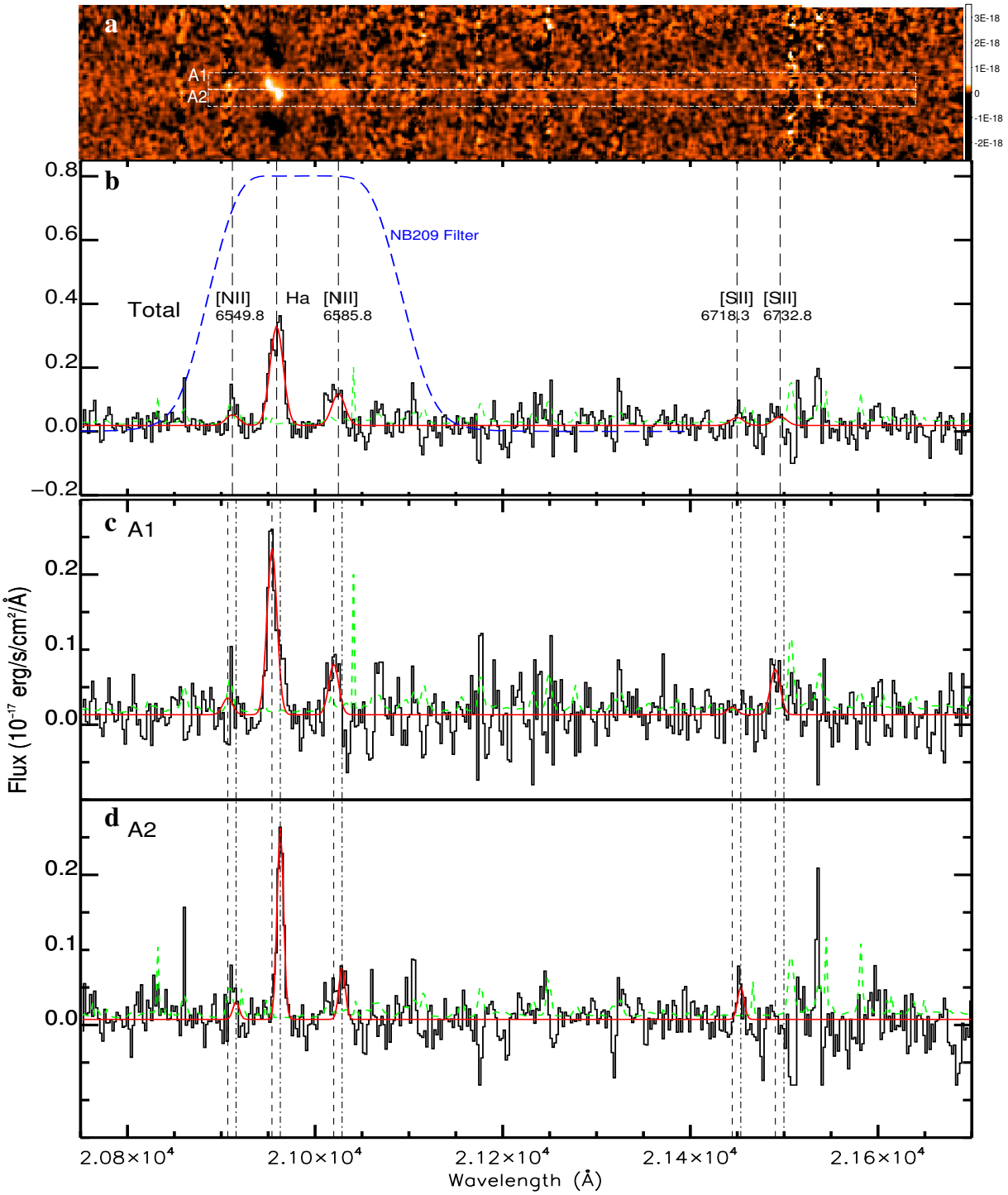

Supplementary Figure 3 – Keck/MOSFIRE spectra of R5519. zoomed in on the wavelength vicinity of Hα, [N II], and [S II] lines. **a,** The 2D spectrum. Long white boxes indicate the two spatial apertures (A1, A2) used to extract two spatially resolved 1D spectra. The spatial length of the box is 8 pixels, corresponding to $\sim 1\farcs4$, about twice the seeing of the observations (thus spatially independent). The flux unit of the colour bar is ergs/s/cm^2/Å. **b,** The total 1D spectrum extracted from the combined aperture of A1 and A2. The blue curve is the filter profile for the FourStar narrow band NB209. **c,** The 1D spectrum extracted from aperture A1. **d,** the 1D spectrum extracted from aperture A2. In all 1D spectra panels, the data, 1-σ, and best-fit Gaussian profiles are shown in black, green, and red, respectively. Vertical long-dashed/short-dashed/dash-dotted lines mark the centroids of the best-fit emission lines from the total/A1/A2 aperture.

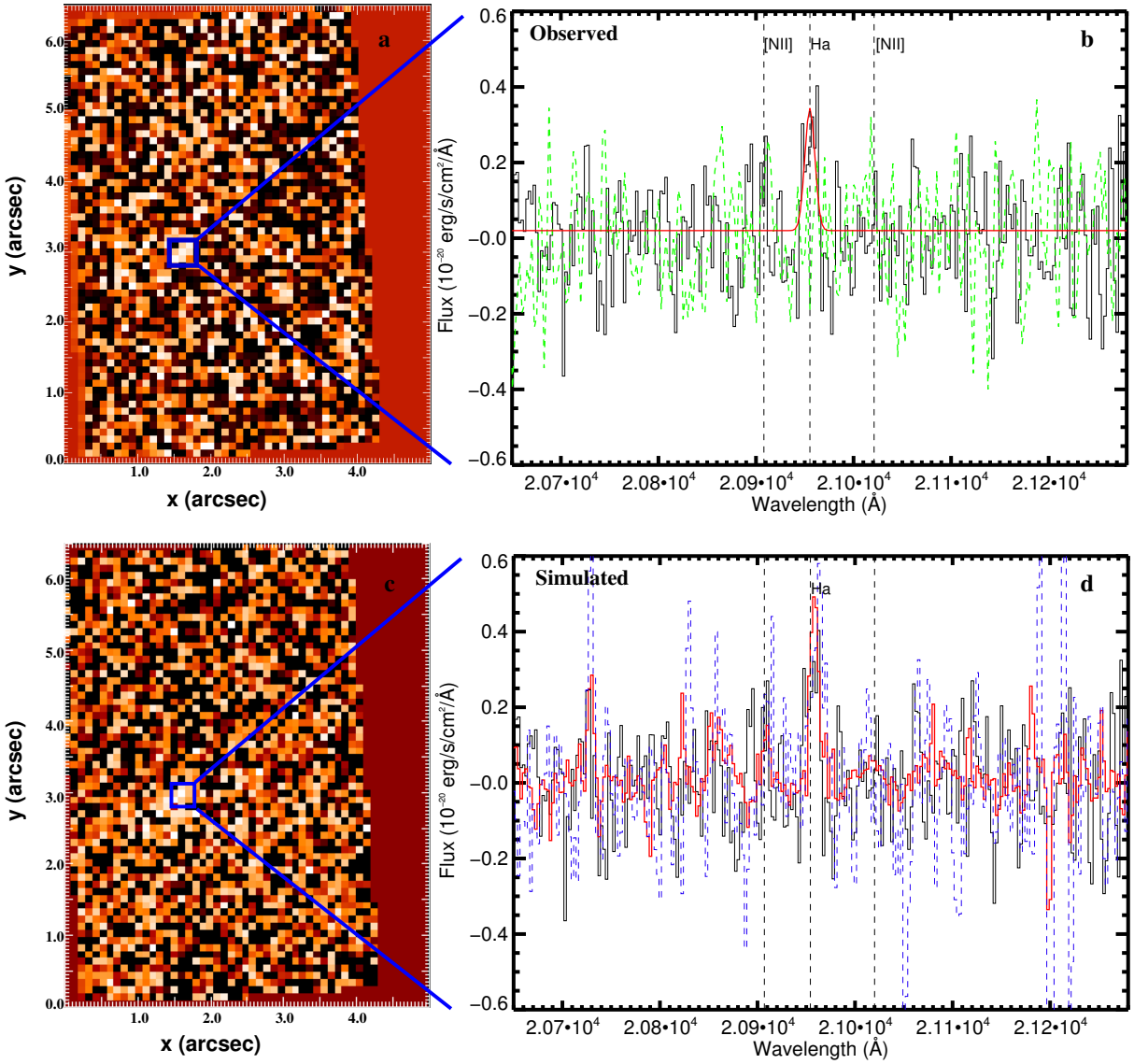

Supplementary Figure 4 – The observed OSIRIS Hα 2D image and simulated Hα detection using the best-fit kinematics and the NB209 narrow-band image of R5519. The flux is calculated for per spaxel, i.e., per 0.01 arcsec^2. **a,** OSIRIS Hα 2D map generated by collapsing the datacube along the wavelength vicinity (20930-21000 Å) of Hα. Most spaxels have no Hα detection (SNR < 1) because of the shallow exposure time. One spatial region shows a robust Hα detection (blue box, 3 by 3 spaxels; 1 spaxel$= 0\farcs1$). The spatial resolution of our AO observation is $\sim 0\farcs35$. **b,** The OSIRIS 1D spectrum averaged over the spatial region (blue box on the left) that shows a Hα detection (SNR $= 4.4$). The data, sky residual and best-fit Gaussian line profile are shown in black, green and red, respectively. Vertical dashed lines indicate the best-fit Hα wavelength centroid and expected [N II] line centroids. The spatial region of the Hα detected provides a key constraint to the kinematic modelling of R5519. **c,** The 2D Hα image from the simulated OSIRIS datacube using the best-fit kinematics and Hα narrow band image. **d,** Simulated OSIRIS 1D spectrum averaged over the same spatial region as the observations. The red line on **d** is an averaged simulated spectrum from 500 iterations. The blue line shows one random iteration from the simulations. The simulation recovers our Hα detection within errors.

Supplementary Table 1 – Ellipse Fit to the Ring Structure

Model (image)	R_{in} kpc (1)	R_{out} kpc (2)	ΔR kpc (3)	R_{ring} kpc (4)	PA $^\circ$ (5)	i $^\circ$ (6)	χ^2/DOF (7)
R5519							
Double Ellipse (F125W+F140W+F160W)	2.7±0.2	6.5±0.2	3.7±0.3	-	28±10	29±5	0.97
Single Ellipse (F125W+F140W+F160W)	-	-	-	5.1±0.4	26±12	29±12	0.54

(1) Best-fit inner semi-major axis for the double ellipse model; (2) Best-fit outer semi-major axis for the double ellipse model; (3) Best-fit width of the ring from the double ellipse model; (4) Average semi-major axis from a single ellipse fit. (5) Best-fit position angle; (6) Best-fit inclination angle; (7) reduced χ^2.

Supplementary Table 2 – Spatially Resolved Aperture Photometry

Photometric Bands	"Nucleus"	Ring region 1	Ring region 2	Ring region 3	Ring average
F125W original (FWHM≈ 0.″26)	26.60±0.07	26.31±0.06	26.08±0.06	26.09±0.06	26.16±0.03
F125W PSF convolved (FWHM≈ 0.″47)	26.53±0.08	26.30±0.05	26.15±0.05	26.26±0.06	26.23±0.03
F160W original (FWHM≈ 0.″26)	25.69±0.06	25.73±0.05	25.70±0.05	25.94±0.05	25.79±0.03
F160W PSF convolved (FWHM≈ 0.″47)	25.72±0.05	25.82±0.05	25.73±0.05	25.96±0.05	25.84±0.03
Ks_{tot} (FWHM≈ 0.″47)	24.86±0.05	25.10±0.05	25.21±0.05	25.58±0.06	25.27±0.03
Colour	"Nucleus"	Ring average			
F125W - F160W (original)	0.91±0.09	0.37±0.04			
F125W - F160W (PSF convolved)	0.82±0.10	0.40±0.04			
F160W - Ks_{tot} (PSF convolved)	0.85±0.07	0.56±0.04			

Magnitudes are in AB units. An aperture with a diameter of 0.″47 is used to measure photometry.

Supplementary Table 3 – MOSFIRE and OSIRIS Emission Line Measurements of R5519

Component	z_s	Line Width km/s	fHα 10^{-17}ergs/s/cm^2	f[N II] -	f[S II]λ6717 -	f[S II]λ6731 -	12+log(O/H) (PP04N2)	12+log(O/H) (D16S2N2)	n_e cm^{-3}
(1)	(2)	(3)	(4)	(5)	(6)	(7)	(8)	(9)	(10)
MOSFIRE Total	2.19273±0.00002	92±1	5.483±0.106	1.770±0.118	0.441±0.096	0.495±0.105	8.62±0.02	8.92±0.06	675^{+455}_{-255}
MOSFIRE A1	2.19197±0.00002	64±1	2.917±0.064	0.894±0.078	<0.301	0.800±0.062	8.61±0.02	8.62±0.07	>5700 (3σ limit)
MOSFIRE A2	2.19332±0.00001	29±2	2.177±0.042	0.596±0.053	0.375±0.041	<0.32[1]	8.57±0.02	8.82±0.07	<210 (3σ limit)
OSIRIS	2.1921±0.0003	64±8	0.42±0.12[2]						

(1) Spatial components as shown in Supplementary Fig.3; (2) Spectroscopic redshifts calculated from the emission line centroid; (3) Emission line Gaussian line width converted to units of velocity dispersion in the rest-frame of the galaxy; (4)-(7) Measured emission line fluxes without aperture or dust correction; (8) Metallicity calculated using the PP04N2 method[19]; (9) Metallicity calculated using the D16S2N2 method[22]; (10) Electron density calculated based on the line ratio of [S II]λ6717 and [S II]λ6731 [ref.[29]]. [1] Uncertain due to the contamination from an OH sky line. [2] Surface brightness in units of 10^{-17}ergs/s/cm^2/″^{2}.

Supplementary Table 4 – Wavelength and PSF dependence of the measured size of the diffuse light

Observed band (approximate rest-frame band)	R_{50} kpc	R_{80} kpc	R_{95} kpc
Ks_{tot} (R), FWHM≈ 0.″47	6.4±0.3	9.9±0.4	13.5±0.6
F125W+F140W+F160W (B), FWHM≈ 0.″26	7.6±0.3	11.8±0.3	15.6±0.6
Ks_{tot} (R) PSF matched, FWHM≈ 0.″9	7.7±0.2	11.8±0.2	16.0±0.6
F125W+F140W+F160W (B) PSF matched, FWHM≈ 0.″9	8.7±0.2	12.8±0.3	16.5±0.6
UBGV stacked (FUV) PSF matched, FWHM≈ 0.″9	9.7±0.2	13.5±0.1	16.0±0.5

The PSF matched images[14] are generated by ZFOURGE using a Moffat profile with FWHM of 0.″9 and $\beta = 0.9$. The rest-frame FUV image is generated by stacking the PSF matched ZFOURGE ground-based optical (UBGV) images.

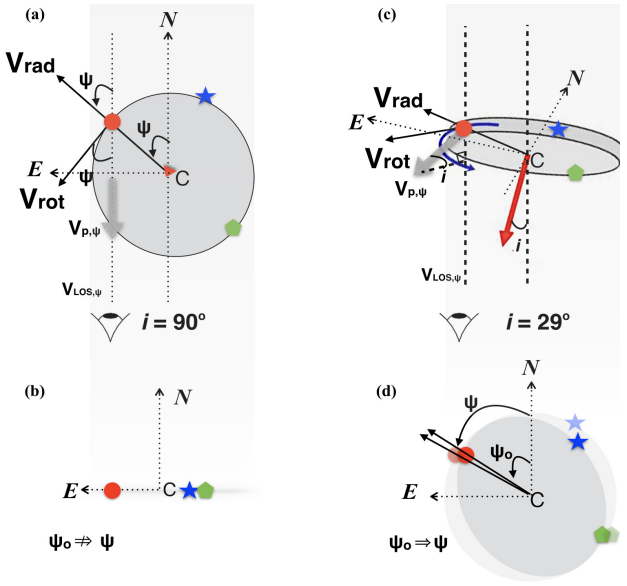

Supplementary Figure 5 – A diagram to illustrate the definitions of variables in Supplementary Information Equations 1-2. Two perpendicular velocity vectors (V_{rad}, V_{rot}) on the ring can be converted to the observed line-of-sight velocity ($V_{LOS,\psi}$) as a function of the observed position angle ψ_o, for inclination angles $i \neq 90°$. ψ_o is defined on the observed 2D image, counterclockwise from the North. **(a),** observing the disk of the ring edge-on ($i = 90°$); the face-on view of the disk is drawn to show the geometry of the expansion velocity (V_{rad}, positive if pointing away from the disk centre C), rotation velocity (V_{rot}, positive if counter-clockwise from the observed North); $V_{p,\psi}$ is the net de-projected 1D velocity on the plane of the disk. $V_{p,\psi}$=$V_{LOS,\psi}$ for an edge-on observation; ψ is the position angle ψ de-projected onto the plane of the ring; the red circle, blue star, and green diamond represent 3 data points on the ring. **(b),** The observed 2D image of **(a)** . The ψ for the 3 data points can not be recovered from ψ_o in this case. **(c),** Similar to Panel (a) but with an inclination angle of e.g., $i = 29°$. **(d),** The observed 2D image of Panel (c); the de-projected ψ can be calculated from the measured ψ_o. The correction from ψ_o to ψ is small for a relatively small i.

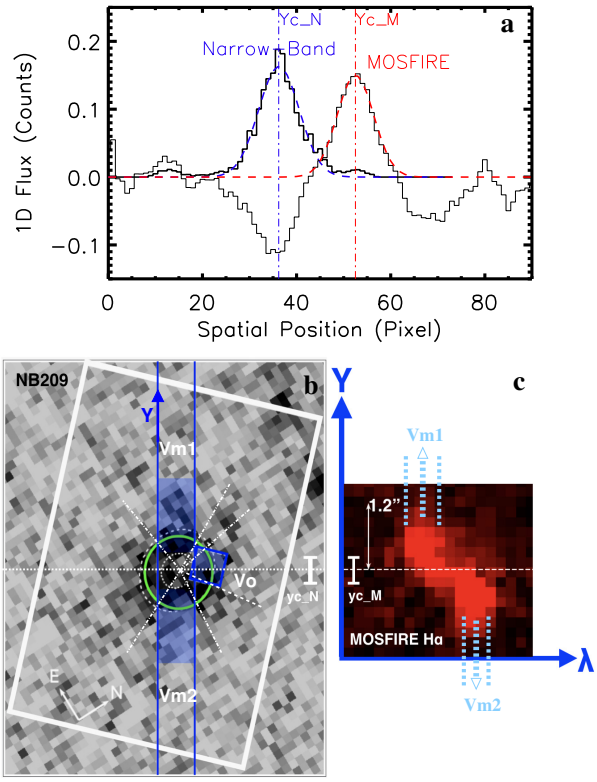

Supplementary Figure 6 – Aligning MOSFIRE and OSIRIS observations on top of the NB209 Hα narrow band image. a, Collapsing the NB209 Hα narrow band flux (black curve) in the direction of the MOSFIRE slit and cross-correlating with the MOSFIRE Hα spatial flux distribution (light black curve). The best-fit Gaussian profiles for the NB209 and the MOSFIRE flux distributions are overlaid in blue dashed and red dashed lines, respectively. The vertical blue and red dot-dashed lines indicate the centroids (Yc_N and Yc_M) of the Gaussian profiles for NB209 and MOSFIRE, respectively. The offset of Yc_N and Yc_M determines the spatial centre of the MOSFIRE 2D spectrum. **b,** The MOSFIRE slit (vertical blue lines), OSIRIS FOV (white box) on top of the NB209 Hα image after alignment. We measure the line-of-sight velocity (V_m1, V_m2, and V_o) for three PAs on the 5 kpc ring (green cirlce). The white dash-dotted lines on the NB209 image show the large error range we consider for our PA measurements. The blue shaded areas show spatial areas where V_m1, V_m2, and V_o are measured from. **c,** The MOSFIRE 2D Hα image aligned to **b,**. The light blue dashed lines on the MOSFIRE Hα image show the error range of V_m1 and V_m2. Given the large errors of the PAs, whether we use the best-fit ellipse (white ellipses) or a circular ring (green circle) do not change the measured velocities noticeably.

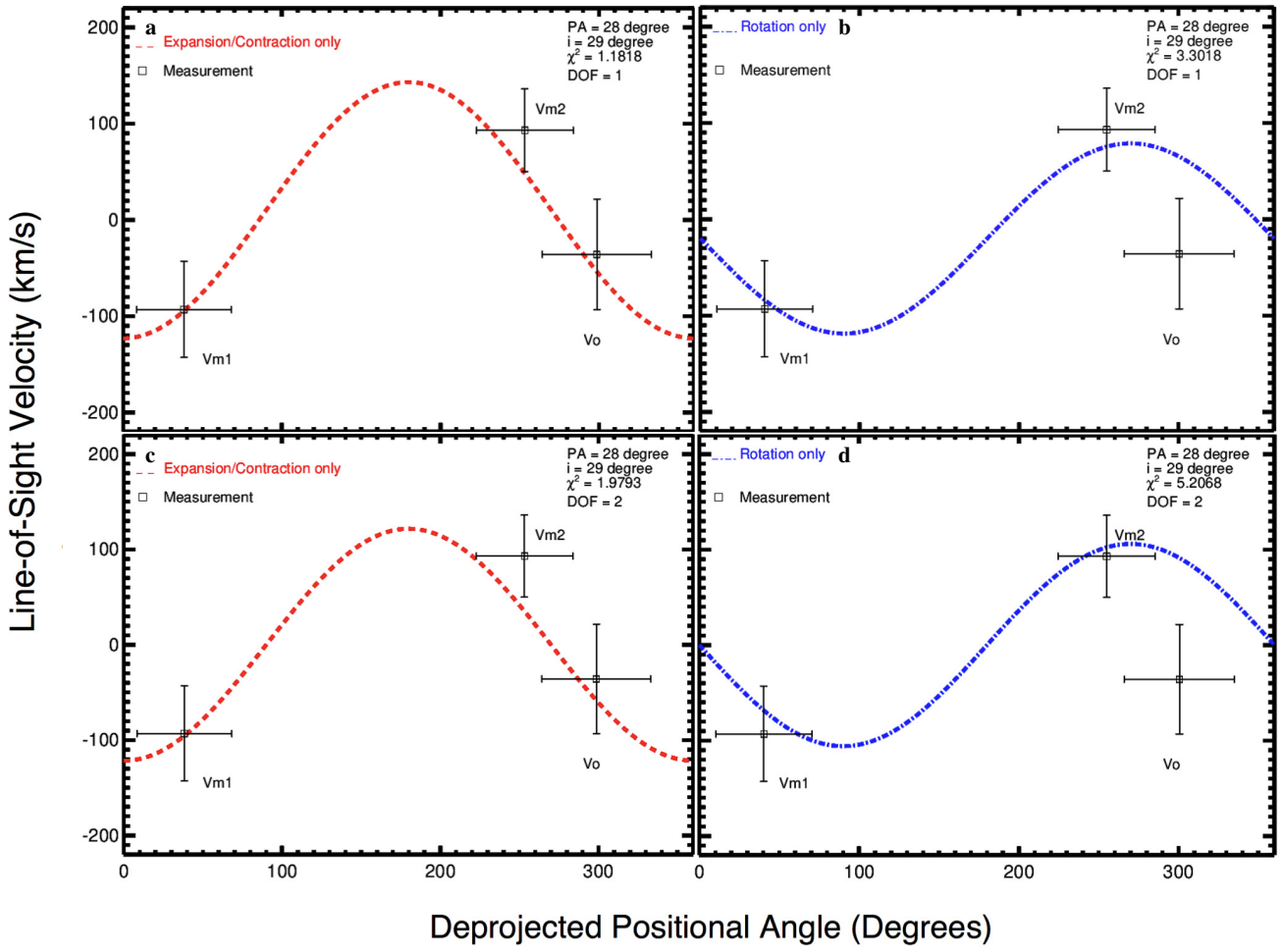

Supplementary Figure 7 – Fitting a rotation only or expansion/contraction only model to the data. The three data points and their uncertainties are the same as Fig.2 in the main text. **a,** Fixing V_{rot} at 0 and fitting the expansion/contraction parameters in Supplementary Eq. 1-2. The red short dashed line shows the best-fit expansion/contraction only model. **b,** Fixing V_{rad} at 0 and fitting the rotational parameters in Supplementary Eq. 1-2. The blue dot-dashed line shows the best-fit rotation only model. For **a** and **b**, we allow the systematic redshift to vary to keep DOF = 1. **c-d,** Similar to **a-b**, but here we fix the systematic redshift at zero.

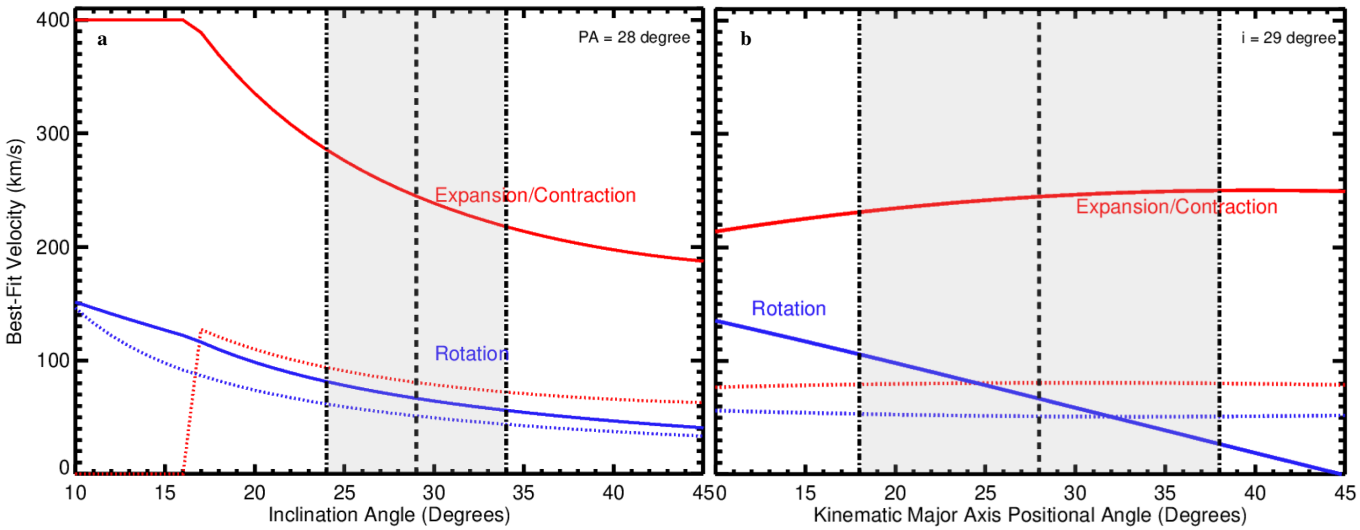

Supplementary Figure 8 – Dependence of the best-fit V_{rot} and V_{rad} on the position angle of the kinematic major axis PA_0 and inclination angle i. **a,** V_{rot} (blue) and V_{rad} (red) as a function of i for a fixed PA_0=29°. **b,** V_{rot} (blue) and V_{rad} (red) as a function of PA_0 for a fixed $i = 29°$. The dotted red/blue curves on both panels indicate the 1σ statistical errors of the fitting. The shaded region highlights the uncertainty range of i and PA_0 from the ellipse fit to images of R5519, with the vertical dashed lines mark the best-fit values and the vertical dot-dashed lines mark the 1σ statistical errors of the best-fit values.

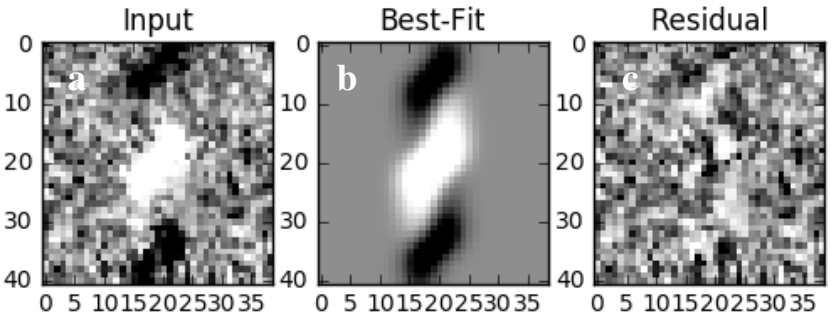

Supplementary Figure 9 – Fitting a simple rotating disk to the MOSFIRE Hα 2D spectrum using HELA[35,36]. In all panels, the y-coordinates are in pixel scales in the spatial direction of the MOSFIRE spectrum and the x-coordinates are in wavelength channels of the spectrum. **a,** Input Hα 2D spectrum. **b,** Best-fit rotating disk model from HELA. **c,** Residual (input data minus the best-fit model).

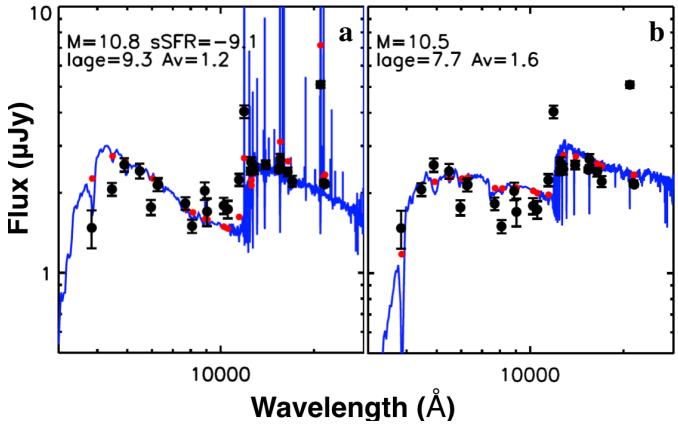

Supplementary Figure 10 – Spectral energy distribution (SED) fitting to the total photometry using two extreme star formation histories (SFHs). **a,** Assuming a constant SFH with emission lines. **b,** Assuming a 10 Myr truncated starburst with no SF afterwards. Black filled circles: observational measurements and associated 1σ statistical errors; red filled circles: modelled flux from the best-fit SED template. Blue curves: best-fit SED models. These two models provide a robust upper and lower limit on the stellar mass and age of R5519.

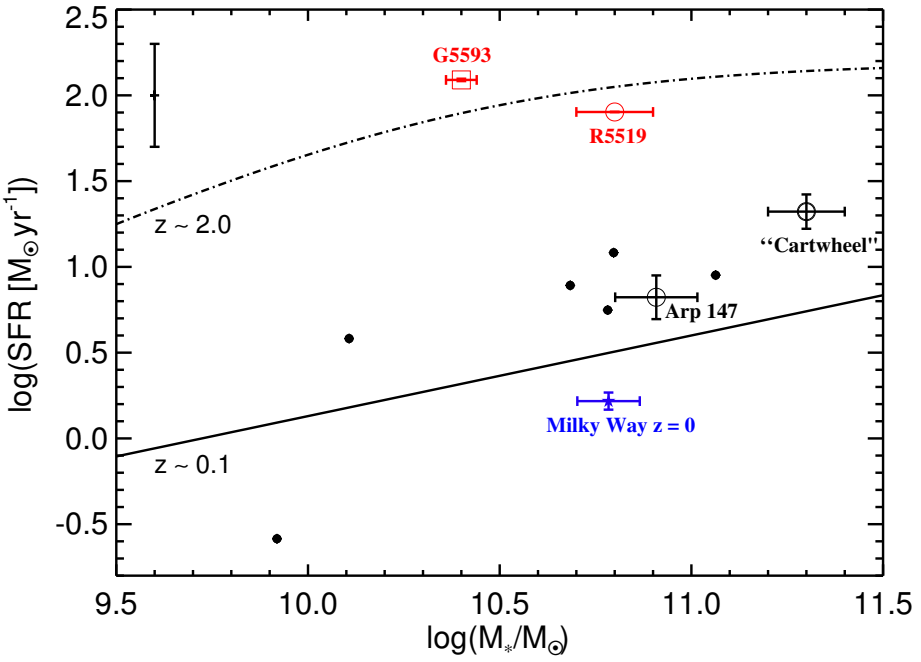

Supplementary Figure 11 – The location of R5519 on the M_*-SFR "main-sequence" relation. The best estimates of M_* and SFR of R5519 (red circle) and its neighbouring galaxy G5593 (red box) are taken from the SED fitting in Table 1. The x-axis errors of R5519 and G5593 are statistical errors presented in Table 1. The y-axis errors of R5519 and G5593 are not shown but are discussed in detail in Methods. The mean M_*-SFR relation[101,102] for $z \sim 2$ and $z \sim 0.1$ galaxies is shown as the dash-dotted and solid line, respectively. The vertical error bar on the top left corner shows the constant ∼0.3 dex scatter of the M_*-SFR relation independent of redshifts[102]. We show the positions of the Milky Way, the nearby CRG Arp 147, and the Cartwheel galaxy for comparison. The data and their associated measurement errors of nearby galaxies and the Milky Way are literature values[43,103–105].

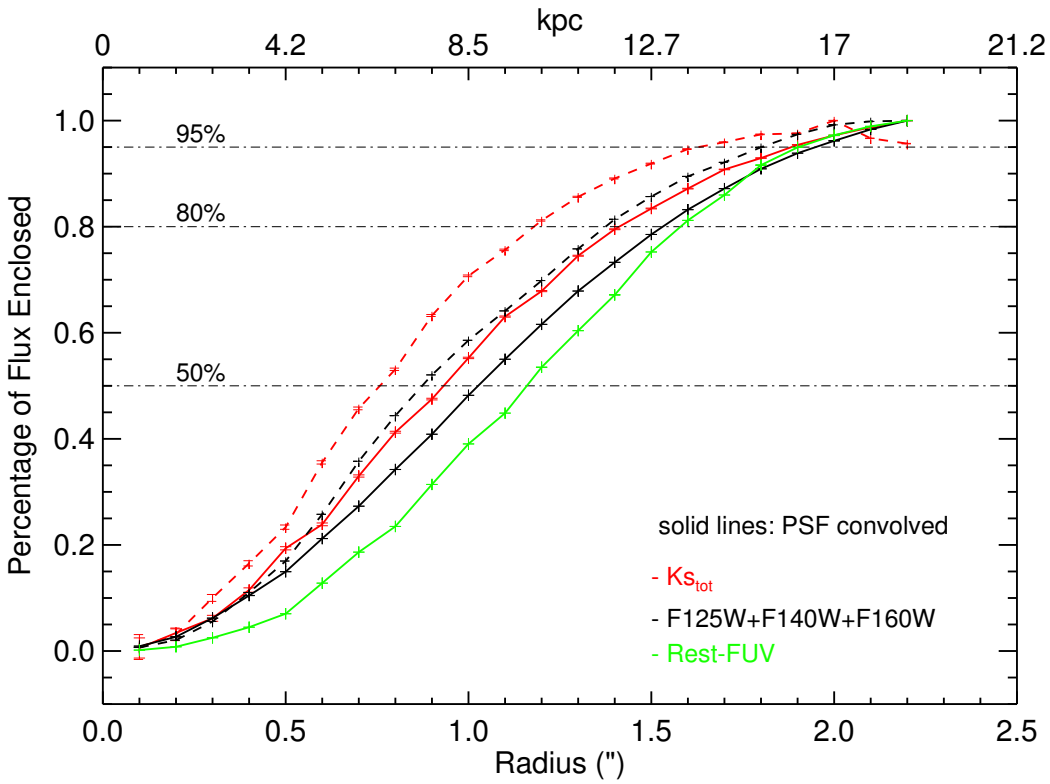

Supplementary Figure 12 – Enclosed total luminosity as a function of radius. The y-axis is the normalised total luminosity within a circular aperture and the x-axis is the projected radius of the aperture. The red, black, and green colours show the measurements on ZFOURGE Ks$_{tot}$, HST F125W+F140W+F160W, and ZFOURGE stacked rest-frame FUV images, respectively. The solid curves are data measured on the PSF-matched images (FWHM $\sim 0.''9$), whereas the dashed lines are data measured on the original images (see also Supplementary Table 4). Horizontal dot-dashed lines indicate the locations where R_{50}, R_{80} and R_{95} are calculated. This figure demonstrates the dependence of our measured R_{50}, R_{80}, and R_{95} on the image resolution and wavelength.

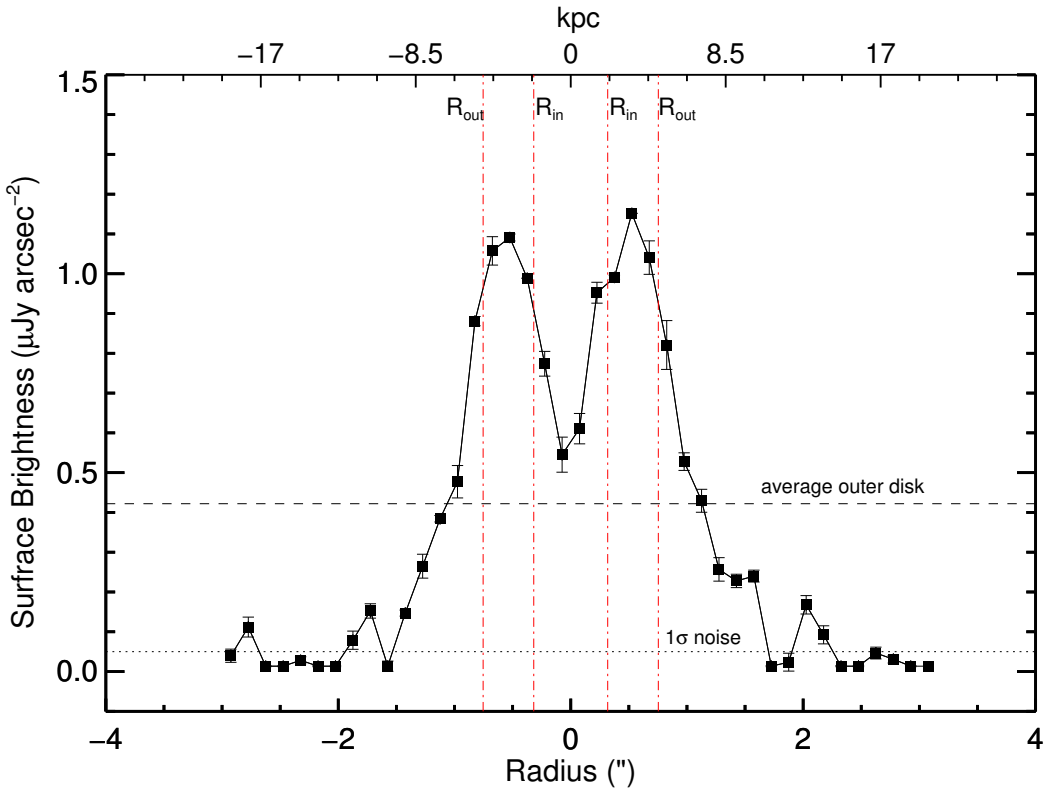

Supplementary Figure 13 – Surface brightness along the major axis of the ring. The 1D surface brightness (SB) is measured on the F160W image along the major axis of the ring ellipse (Supplementary Fig.1). The left-hand side (R<0) corresponds to the North-East side of the slice in Supplementary Fig.1. Three slices (solid and dashed red lines in Supplementary Fig.1) across the ellipse and along the major axis are averaged with each datapoint represents one resolution element ($\sim 0\farcs26$) of the image. The error of each datapoint represents the 1σ standard deviation of the mean. The 1σ image background noise is shown as the horizontal dotted line. The total size of R5519 as measured where the SB drops to the 1σ noise level is 14-16 kpc, which is consistent with our measured R_{95} using the circular aperture on the combined F125W+F140W+F160W HST image (Supplementary Table 4). Vertical red dash-dotted lines show the best-fit inner and outer ring radius (R_{in}, R_{out}) from the the double ellipse fit in Supplementary Fig.1. Alternatively, R_{in} and R_{out} can be measured based on the 1D SB profile (Method). We find R_{in}=2.1 kpc and R_{out}=2.1 kpc, broadly consistent with the 2D double ellipse fit (Supplementary Table 1). The average SB of the outer diffuse disk (R_{out}=6.7 kpc $<R<$ R_{95}=16 kpc) is $\sim$0.42 μJy arcsec^{-2}. Changing the baseline of the FWHM to the average SB of the diffuse disk yields a $\sim$0.5 kpc increase/decrease in R_{in}/R_{out}.

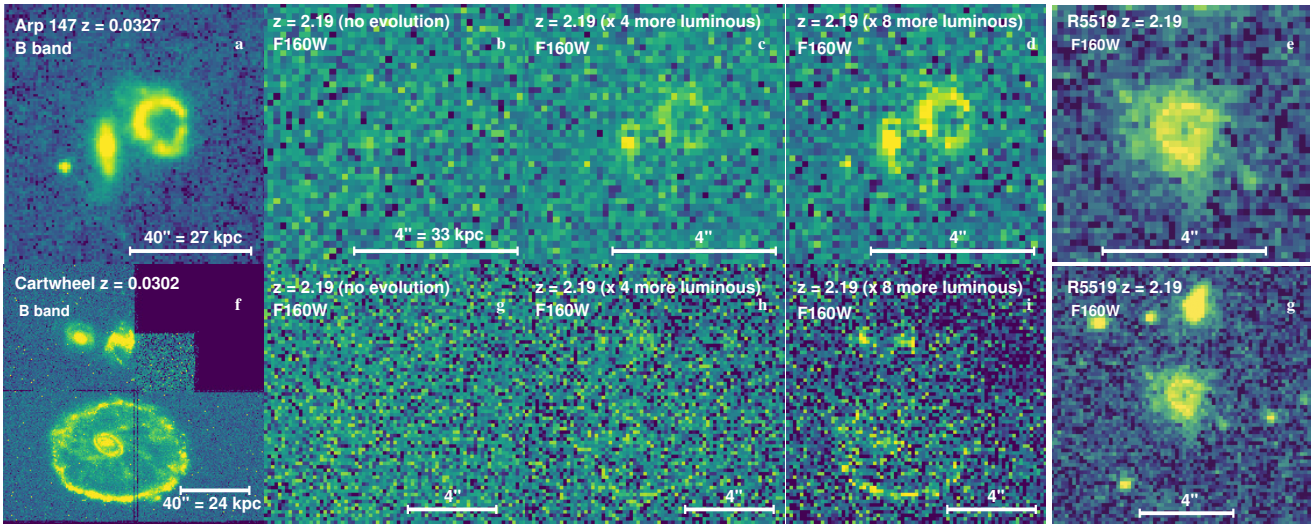

Supplementary Figure 14 – Simulating the F160W morphology of Arp 147 and Cartwheel at $z = 2.19$. **a,** The ground-based B-band image of a local CRG - Arp 147. **b-d,** Simulated image of Arp 147 in the HST F160W band for the limiting magnitude of our current observations. **b** assumes there is no evolution in the intrinsic properties of Arp 147. **c** and **d** assume that the intrinsic rest-frame B-band luminosity is increased by a factor of 4 and 8, respectively. **e,** Observed HST F160W image of R5519, zoomed to show the same field of view as Arp 147. **f,** The HST B-band image of a local CRG - the Cartwheel galaxy. **g-i,** Simulated image of Cartwheel in the HST F160W band for the limiting magnitude of our current observations. **g** assumes there is no evolution in the intrinsic properties of Cartwheel. **h** and **i** assume that the intrinsic rest-frame B-band luminosity is increased by a factor of 4 and 8, respectively. **g,** Observed HST F160W image of R5519, zoomed to show the same field of view as the Cartwheel galaxy.

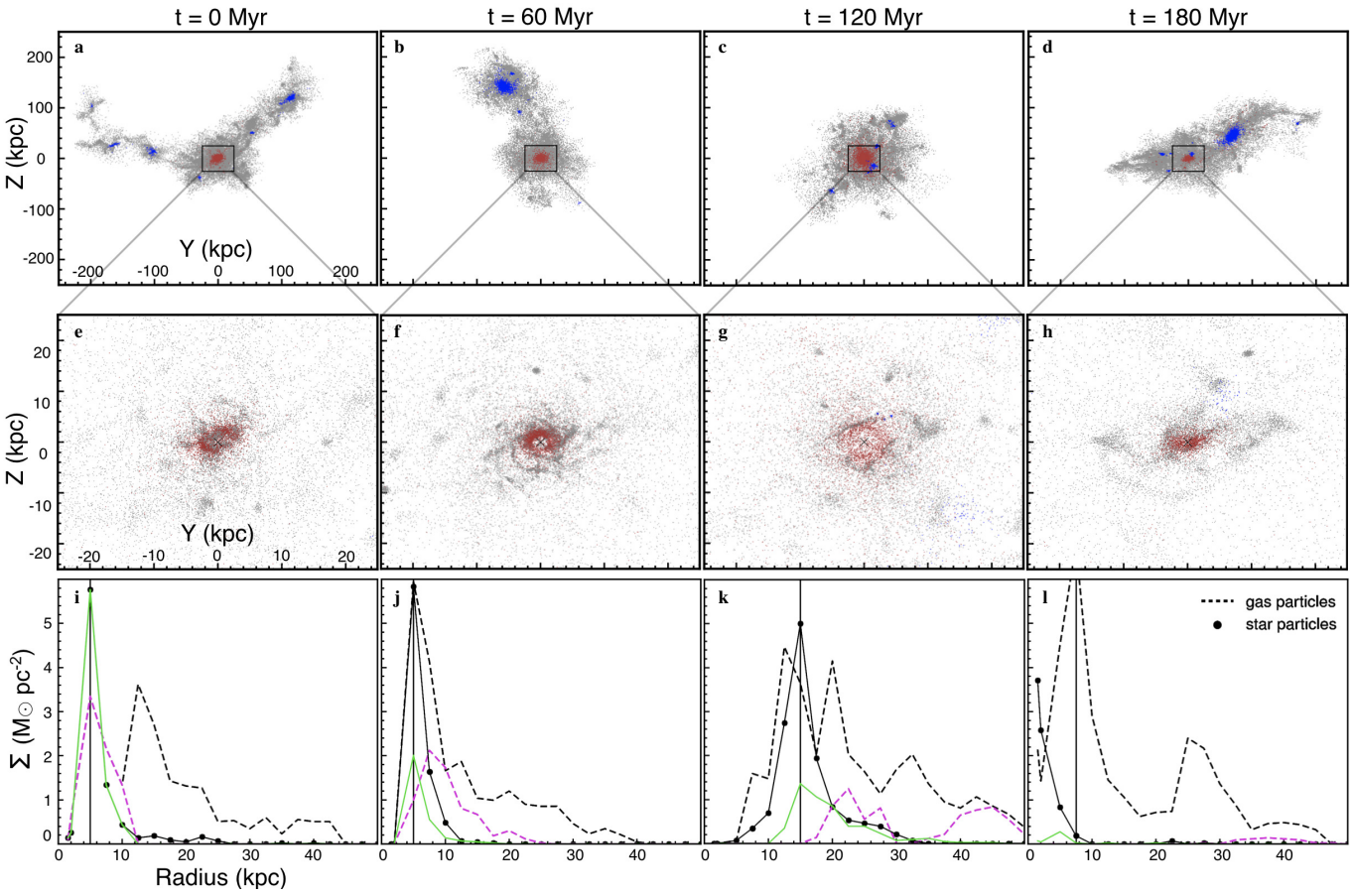

Supplementary Figure 15 – The time evolution of a CRG at $z = 2.23$ from the EAGLE cosmological hydrodynamical simulations[47]. The four columns from left to right denote four time "snipshots"[46] with respect to an arbitrarily defined ring formation time ($t = 0$ Myr). "Snipshots" are defined in the EAGLE simulations as having finer time resolution than snapshots. **a-d,** A 500×500 kpc view, through the simulation Z−Y axes, of the large scale environment in 2D centred on the ring host; red-brown = host galaxy stars, blue = satellite halo stars, and grey=gas particles. **e-h,** A 50×50kpc zoom-in view of the ring host in 2D, red-brown = young stars with ages < 100 Myr, and grey=gas. **i-l,** The surface mass density for star and gas particles (excluding those from the nucleus) at each radius. The location of the ring feature is defined as the peak of the star particle surface mass density. The green and purple lines show the location of the ring's star and gas particles identified at $t = 0$ Myr, respectively, and the positions of these particles with radius in the subsequent "snipshots". In a later time "snipshot" at $t = 240$ Myr (not shown here), the nucleus of the CRG is found to be broken into two parts after the major merger at $t = 180$ Myr .

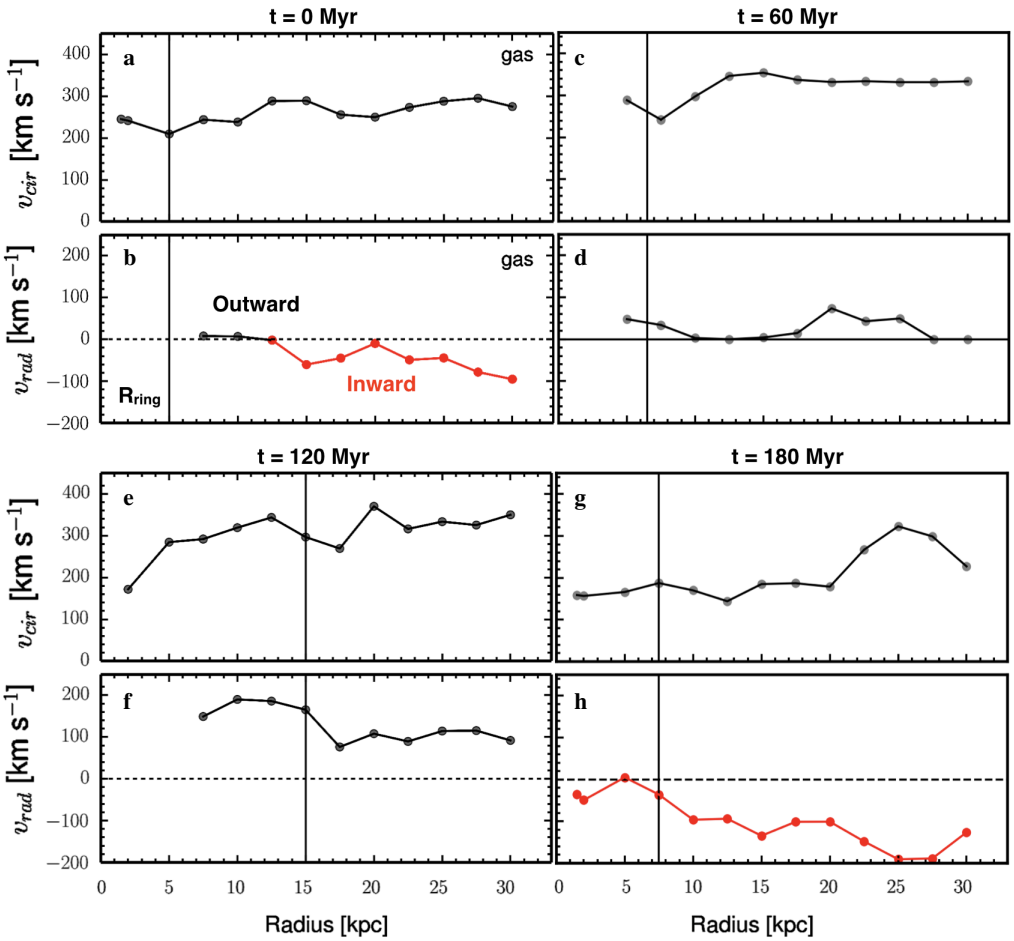

Supplementary Figure 16 – The circular and radial velocity of the gas particles in the $z = 2.23$ EAGLE CRG. a-h, We show four time "snipshots" with respect to an arbitrarily defined ring formation time ($t = 0$ Myr). For each time "snipshot", the circular and radial velocity are shown in the upper and lower panels, respectively. This CRG is expanding from $t = 0$ Myr to 120 Myr, but the ring feature is disrupted due to a second passage of a satellite galaxy at time 180 Myr. During these four time snipshots the radius of this CRG ring (defined as the peak of the 1D surface mass density of the stars; see Supplementary Fig.14) also changes from 5, 6.5, 15, to 7.5 kpc, respectively. The red colour highlights the particle radial velocity that is moving towards the centre of the CRG host.